

Quasar Quartet Embedded in Giant Nebula Reveals Rare Massive Structure in Distant Universe

Joseph F. Hennawi^{1,*}, J. Xavier Prochaska², Sebastiano Cantalupo^{2,3},
Fabrizio Arrigoni-Battaia¹

¹Max-Planck-Institut für Astronomie, Königstuhl, Germany

²University of California Observatories-Lick Observatory, UC Santa Cruz, CA

³ETH Zurich, Institute of Astronomy, Zurich, Switzerland

*To whom correspondence should be addressed; E-mail: joe@mpia.de

All galaxies once passed through a hyper-luminous quasar phase powered by accretion onto a supermassive black hole. But because these episodes are brief, quasars are rare objects typically separated by cosmological distances. In a survey for Lyman- α emission at redshift $z \approx 2$, we discovered a physical association of four quasars embedded in a giant nebula. Located within a substantial overdensity of galaxies, this system is likely the progenitor of a massive galaxy cluster. The chance probability of finding a quadruple-quasar is estimated to be $\sim 10^{-7}$, implying a physical connection between Lyman- α nebulae and the locations of rare protoclusters. Our findings imply that the most massive structures in the distant Universe have a tremendous supply ($\simeq 10^{11}$ solar masses) of cool dense (volume density $\simeq 1 \text{ cm}^{-3}$) gas, in conflict with current cosmological simulations.

Cosmologists do not fully understand the origin of supermassive black holes (SMBHs) at the centers of galaxies, and how they relate to the evolution of the underlying dark matter, which forms the backbone for structure in the Universe. In the current paradigm, SMBHs grew in every massive galaxy during a luminous quasar phase, making distant quasars the progenitors of the dormant SMBHs found at the centers of nearby galaxies. Tight correlations between the masses of these local SMBHs and both their host galaxy (1) and dark matter halo masses (2) support this picture, further suggesting that the most luminous quasars at high-redshift should reside in the most massive galaxies. It has also been proposed that quasar activity is triggered by the frequent mergers that are a generic consequence of hierarchical structure formation (3, 4). Indeed, an excess in the number of small-separation binary quasars (5, 6), as well as the mere

existence of a handful of quasar triples (7, 8), support this hypothesis. If quasars are triggered by mergers, then they should preferentially occur in rare peaks of the density field, where massive galaxies are abundant and the frequency of mergers is highest (9).

Following these arguments, one might expect that at the peak of their activity $z \sim 2 - 3$, quasars should act as signposts for protoclusters, the progenitors of local galaxy clusters and the most massive structures at that epoch. However, quasar clustering measurements (10, 11) indicate that quasar environments at $z \sim 2 - 3$ are not extreme: these quasars are hosted by dark matter halos with masses $M_{\text{halo}} \sim 10^{12.5} M_{\odot}$ (where M_{\odot} is the mass of the Sun), too small to be the progenitors of local clusters (12). But the relationship between quasar activity and protoclusters remains unclear, owing to the extreme challenge of identifying the latter at high-redshift. Indeed, the total comoving volume of even the largest surveys for distant galaxies at $z \sim 2 - 3$ is only $\sim 10^7 \text{ Mpc}^3$, which would barely contain a single rich cluster locally.

Protoclusters have been discovered around a rare-population of active galactic nuclei (AGN) powering large-scale radio jets, known as high-redshift radio galaxies (HzRGs) (13). The HzRGs routinely exhibit giant $\sim 100 \text{ kpc}$ nebulae of luminous $\text{Ly}\alpha$ emission $L_{\text{Ly}\alpha} \sim 10^{44} \text{ erg s}^{-1}$. Nebulae of comparable size and luminosity have also been observed in a distinct population of objects known as ‘ $\text{Ly}\alpha$ blobs’ (LABs) (14, 15). The LABs are also frequently associated with AGN activity (16–18), although lacking powerful radio jets, and appear to reside in overdense, protocluster environments (15, 19, 20). Thus among the handful of protoclusters (21) known, most appear to share two common characteristics: the presence of an active SMBH and a giant $\text{Ly}\alpha$ nebula.

We have recently completed a spectroscopic search for extended $\text{Ly}\alpha$ emission around a sample of 29 luminous quasars at $z \sim 2$, each the foreground (f/g) member of a projected quasar pair (22). Analysis of spectra from the background (b/g) members in such pairs reveals that quasars exhibit frequent absorption from a cool, metal-enriched, and often optically thick medium on scales of tens to hundreds kpc (22–28). The UV radiation emitted by the luminous f/g quasar can, like a flashlight, illuminate this nearby neutral hydrogen, and power a large-scale $\text{Ly}\alpha$ -emission nebula, motivating our search. By construction, our survey selects for exactly the two criteria which seem to strongly correlate with protoclusters: an active SMBH and the presence of a large-scale $\text{Ly}\alpha$ emission nebula.

Of the 29 quasars surveyed, only SDSSJ0841+3921 exhibited extended large-scale ($\gtrsim 50 \text{ kpc}$) $\text{Ly}\alpha$ emission above our characteristic sensitivity limit of $6 \times 10^{-18} \text{ erg s}^{-1} \text{ cm}^{-2} \text{ arcsec}^{-2}$ (2σ). We designed a custom narrow-band filter tuned to the wavelength of $\text{Ly}\alpha$ at the f/g quasar redshift $z = 2.0412$ ($\lambda_{\text{center}} = 3700\text{\AA}$, $\text{FWHM}_{\lambda} = 33\text{\AA}$), and imaged the field with the Keck/LRIS imaging spectrometer for 3hrs on UT 12 November 2012. The combined and processed images reveal $\text{Ly}\alpha$ emission from a giant filamentary structure centered on the f/g quasar and extending continuously towards the b/g quasar (see Fig. 1). This nebula has an end-to-end size of $37''$ corresponding to 310 kpc and a total line luminosity $L_{\text{Ly}\alpha} = 2.1 \times 10^{44} \text{ erg s}^{-1}$, making it one of the largest and brightest nebula ever discovered.

The giant nebula is only one of the exceptional properties of SDSSJ 0841+3921. Our images reveal three relatively compact candidate $\text{Ly}\alpha$ emitting sources with faint continuum

magnitudes $V \simeq 23 - 24$, embedded in the $\text{Ly}\alpha$ filament and roughly aligned with its major axis. Follow-up spectroscopy reveals that the sources labeled AGN1, AGN2, and AGN3 are three AGN at the same redshift as the f/g quasar (see right panel of Fig. 1 and (29)), making this system the only quadruple AGN known. Adopting recent measurements of small-scale quasar clustering (30), we estimate that the probability of finding three AGN around a quasar with such small separations is $\sim 10^{-7}$ (31). Why then did we discover this rare coincidence of AGN in a survey of just 29 quasars? Did the giant nebula mark the location of a protocluster with dramatically enhanced AGN activity?

To test this hypothesis, we constructed a catalog of $\text{Ly}\alpha$ -emitting galaxies (LAEs), and computed the cumulative overdensity profile of LAEs around SDSSJ0841+3921, relative to the background number expected based on the LAE luminosity function (32) (see Fig. 2). To perform a quantitative comparison to other giant $\text{Ly}\alpha$ nebulae, many of which are known to coincide with protoclusters, we measured the giant nebulae-LAE cross-correlation function for a sample of eight systems – six HzRGs and two LABs – for which published data was available in the literature (33). In Fig. 2, we compare the overdensity profile around SDSSJ0841+3921 to this giant nebulae-LAE correlation function. On average, the environment of HzRGs and LABs hosting giant $\text{Ly}\alpha$ nebulae (red line) is much richer than that of radio-quiet quasars (10) (blue line), confirming that they indeed reside in protoclusters. Furthermore, the clustering of LAEs around SDSSJ0841+3921 has a steeper overdensity profile, and exceeds the average protocluster by a factor of $\gtrsim 20$ for $R < 200$ kpc and by ~ 3 on scales of $R \simeq 1$ Mpc. In addition to the overdensity of four AGN, the high number of LAEs surrounding SDSSJ0841+3921 make it one of the most overdense protoclusters known at $z \sim 2 - 3$.

The combined presence of several bright AGN, the $\text{Ly}\alpha$ emission nebula, and the b/g absorption spectrum, provide an unprecedented opportunity to study the morphology and kinematics of the protocluster via multiple tracers, and we find evidence for extreme motions (34). Specifically, AGN1 is offset from the precisely determined systemic redshift (35) of the f/g quasar by $+1300 \pm 400 \text{ km s}^{-1}$. This large velocity offset cannot be explained by Hubble expansion – the miniscule probability of finding a quadruple quasar in the absence of clustering $P \sim 10^{-13}$ (31) and the physical association between the AGN and giant nebula demand that the four AGN reside in a real collapsed structure – and thus provides an unambiguous evidence for extreme gravitational motions. In addition, our slit spectra of the giant $\text{Ly}\alpha$ nebula reveal extreme kinematics of diffuse gas (Fig. 3), extending over a velocity range of -800 to $+2500 \text{ km s}^{-1}$ from systemic. Furthermore, there is no evidence for double-peaked velocity profiles characteristic of resonantly-trapped $\text{Ly}\alpha$, which could generate large velocity widths in the absence of correspondingly large gas motions. Absorption line kinematics of the metal-enriched gas, measured from the b/g quasar spectrum at impact parameter of $R_{\perp} = 176$ kpc (Fig. 4), show strong absorption at $\approx +650 \text{ km s}^{-1}$ with a significant tail to velocities as large as $\simeq 1000 \text{ km s}^{-1}$. It is of course possible that the extreme gas kinematics, traced by $\text{Ly}\alpha$ emission and metal-line absorption, are not gravitational but rather arise from violent large-scale outflows powered by the multiple AGN. While we cannot completely rule out this possibility, the large velocity offset of $+1300 \text{ km s}^{-1}$ between the f/g quasar and the emission redshift of AGN1 can only result from

gravity.

One can only speculate about the origin of the dramatic enhancement of AGN in the SDSSJ0841+3921 protocluster. Perhaps the duty cycle for AGN activity is much longer in protoclusters, because of frequent dissipative interactions (5, 6), or an abundant supply of cold gas. A much larger number of massive galaxies could also be the culprit, as AGN are known to trace massive halos at $z \sim 2$. Although SDSSJ0841+3921 is the only example of a quadruple AGN with such small separations, previously studied protoclusters around HzRGs and LABs, also occasionally harbor multiple AGN (13, 36). Regardless, our discovery of a quadruple AGN and protocluster from a sample of only 29 quasars suggests a link between giant Ly α nebulae, AGN activity, and protoclusters – similar to past work on HzRGs and LABs – with the exception that SDSSJ 0841+3921 was selected from a sample of normal radio-quiet quasars. From our survey and other work (37), we estimate that $\simeq 10\%$ of quasars exhibit comparable giant Ly α nebulae. Although clustering measurements imply that the majority of $z \sim 2$ quasars reside in moderate overdensities (10–12), we speculate that this same 10% trace much more massive protoclusters. SDSSJ0841+3921 clearly supports this hypothesis, as does another quasar-protocluster association (10, 38), around which a giant Ly α nebula was recently discovered (39, 40).

Given our current theoretical picture of galaxy formation in massive halos, an association between giant Ly α nebulae and protoclusters is completely unexpected. The large Ly α luminosities of these nebulae imply a substantial mass ($\sim 10^{11} M_\odot$) of cool ($T \sim 10^4$ K) gas (41), whereas cosmological hydrodynamical simulations indicate that already by $z \sim 2 - 3$, baryons in the massive progenitors ($M_{\text{halo}} \gtrsim 10^{13} M_\odot$) of present-day clusters are dominated by a hot shock-heated plasma $T \sim 10^7$ K (42, 43). These hot halos are believed to evolve into the X-ray emitting intra-cluster medium observed in clusters, for which absorption-line studies indicate negligible $\lesssim 1\%$ cool gas fractions (44). Clues about the nature of this apparent discrepancy come from our absorption line studies of the massive $\simeq 10^{12.5} M_\odot$ halos hosting $z \sim 2 - 3$ quasars. This work reveals substantial reservoirs of cool gas $\gtrsim 10^{10} M_\odot$ (22–28), manifest as a high covering factor $\simeq 50\%$ of optically thick absorption, several times larger than predicted by hydrodynamical simulations (42, 43). This conflict most likely indicates that current simulations fail to capture essential aspects of the hydrodynamics in massive halos at $z \sim 2$ (27, 42), perhaps failing to resolve the formation of clumpy structure in cool gas (41).

If illuminated by the quasar, these large cool gas reservoirs in the quasar circumgalactic medium (CGM) will emit fluorescent Ly α photons, and we argue that this effect powers the nebula in SDSSJ0841+3921 (45). But according to this logic, nearly every quasar in the Universe should be surrounded by a giant Ly α nebulae with size comparable to its CGM (~ 200 kpc). Why then are these giant nebulae not routinely observed?

This apparent contradiction can be resolved as follows. If this cool CGM gas is illuminated and highly ionized, it will fluoresce in the Ly α line with a surface brightness scaling as $\text{SB}_{\text{Ly}\alpha} \propto N_{\text{H}} n_{\text{H}}$, where N_{H} is the column density of cool gas clouds which populate the quasar halo, and n_{H} is the number density of hydrogen atoms inside these clouds. Note the total cool gas mass of the halos scales as $M_{\text{cool}} \propto R^2 N_{\text{H}}$, where R is the radius of the halo (45). Given our best estimate for the properties of the CGM around typical quasars ($n_{\text{H}} \sim 0.01 \text{ cm}^{-3}$

and $N_{\text{H}} \sim 10^{20} \text{ cm}^{-2}$ or $M_{\text{cool}} \simeq 10^{11} M_{\odot}$) (22, 26, 27), we expect these nebulae to be extremely faint $\text{SB}_{\text{Ly}\alpha} \sim 10^{-19} \text{ erg s}^{-1} \text{ cm}^{-2} \text{ arcsec}^{-2}$, and beyond the sensitivity of current instruments (22). One comes to a similar conclusion based on a full radiative transfer calculation through a simulated dark-matter halo with mass $M_{\text{halo}} \approx 10^{12.5} M_{\odot}$ (41). Thus the factor of ~ 100 times larger surface brightness observed in the SDSSJ0841+3921 and other protocluster nebulae, arises from either a higher n_{H} , N_{H} (and hence higher M_{cool}), or both. The cool gas properties required to produce the SDSSJ0841+3921 nebula can be directly compared to those deduced from an absorption line analysis of the b/g quasar spectrum (46).

The b/g quasar sightline pierces through SDSSJ0841+3921 at an impact parameter of $R_{\perp} = 176 \text{ kpc}$, giving rise to the absorption spectrum shown in Fig. 4. Photoionization modeling of these data constrains the total hydrogen column density to be $\log_{10} N_{\text{H}} = 20.4 \pm 0.4$ (45), implying a substantial mass of cool gas $1.0 \times 10^{11} M_{\odot} < M_{\text{cool}} < 6.5 \times 10^{11} M_{\odot}$ within $r = 250 \text{ kpc}$. Assuming that the Ly α emitting gas has the same column density as the gas absorbing the b/g sightline, reproducing the large fluorescent Ly α surface brightness requires that this gas be distributed in compact $r_{\text{cloud}} \sim 40 \text{ pc}$ clouds at densities characteristic of the interstellar medium $n_{\text{H}} \simeq 2 \text{ cm}^{-3}$, but on $\sim 100 \text{ kpc}$ scales in the protocluster.

Clues to the origin of these dense clumps of cool gas comes from their high enrichment level, which we have determined from our absorption line analysis (46) to be greater than 1/10th of the solar value. At first glance, this suggests that strong tidal interactions due to merger activity or outflows due to powerful AGN feedback are responsible for dispersing dense cool gas in the protocluster. However, the large cool gas mass $\sim 10^{11} M_{\odot}$ and high velocities $\sim 1000 \text{ km s}^{-1}$, imply an extremely large kinetic luminosity $L_{\text{wind}} \sim 10^{44.6}$ for an AGN powered wind, making the feedback scenario implausible (25). An even more compelling argument against a merger or feedback origin comes from the extremely small cloud sizes $r_{\text{cloud}} \sim 40 \text{ pc}$ implied by our measurements. Such small clouds moving supersonically $\sim 1000 \text{ km s}^{-1}$ through the hot $T \sim 10^7 \text{ K}$ shock-heated plasma predicted to permeate the protocluster, will be disrupted by hydrodynamic instabilities in $\sim 5 \times 10^6 \text{ yr}$, and can thus only be transported $\sim 5 \text{ kpc}$ (47). These short disruption timescales instead favor a scenario where cool dense clouds are formed in situ, perhaps via cooling and fragmentation instabilities, but are short-lived. The higher gas densities might naturally arise if hot plasma in the incipient intra-cluster medium pressure confines the clouds, compressing them to high densities (48, 49). Emission line nebulae from cool dense gas has also been observed at the centers of present-day cooling flow clusters (50, 51), albeit on much smaller scales $\lesssim 50 \text{ kpc}$. The giant Ly α nebulae in $z \sim 2 - 3$ protoclusters might be manifestations of the same phenomenon, but with much larger sizes and luminosities, reflecting different physical conditions at high-redshift.

The large reservoir of cool dense gas in the protocluster SDSSJ0841+3921, as well as those implied by the giant nebulae in other protoclusters, appear to be at odds with our current theoretical picture of how clusters form. This is likely symptomatic of the same problem of too much cool gas in massive halos already highlighted for the quasar CGM (27, 42, 43). Progress will require more cosmological simulations of massive halos $M \gtrsim 10^{13} M_{\odot}$ at $z \sim 2$, as well as idealized higher-resolution studies. In parallel, a survey for extended Ly α emission around

~ 100 quasars would uncover a sample of ~ 10 giant $\text{Ly}\alpha$ nebulae likely coincident with protoclusters, possibly also hosting multiple AGN, and enabling continued exploration of the relationship between AGN, cool gas, and cluster progenitors.

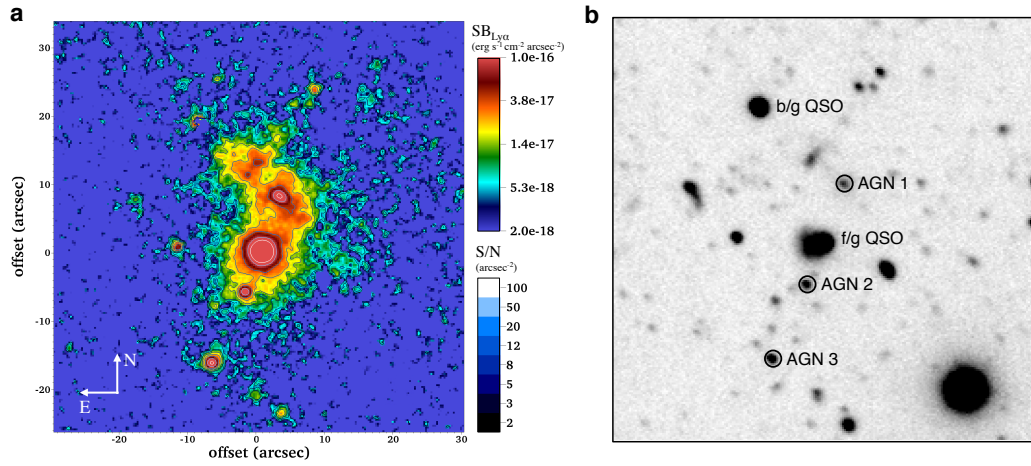


Fig. 1: Narrow and broad band images of the field surrounding SDSSJ0841+3921 **Left:** Continuum-subtracted, narrow-band image of the field around f/g quasar. The color map and the contours indicate the $\text{Ly}\alpha$ surface brightness (upper color bar) and the signal-to-noise ratio per arcsec^2 aperture (lower color bar), respectively. This image reveals a giant $\text{Ly}\alpha$ nebula on the northern side of the f/g quasar and several compact, bright $\text{Ly}\alpha$ emitters in addition to the f/g quasar. Three of these have been spectroscopically confirmed as active galactic nuclei (AGN) at the same redshift. **Right:** Corresponding V -band continuum image of the field presented at left with the locations of the four AGN marked. The AGN are roughly oriented along a line coincident with the projected orientation of the $\text{Ly}\alpha$ nebula. We also mark the position of the b/g quasar, which is not physically associated with the quadruple AGN system, but whose absorption spectrum probes the gaseous environment of the f/g quadruple AGN and protocluster (see Fig. 4).

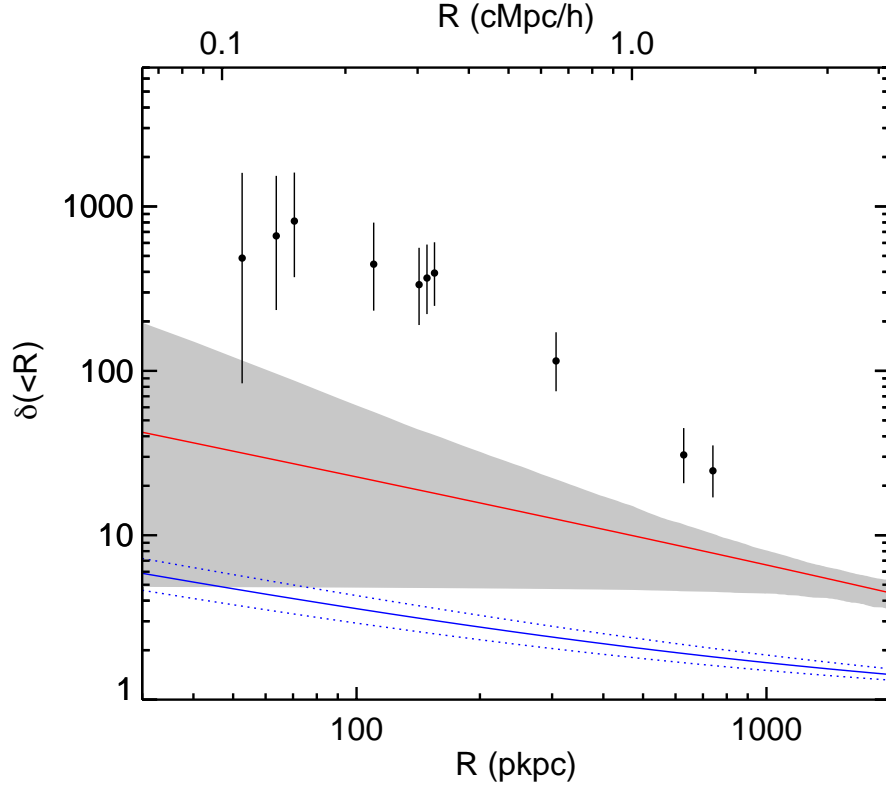


Fig. 2: Characterization of the protocluster environment around SDSSJ0841+3921 . The data points indicate the cumulative overdensity profile of LAEs $\delta(< R)$ as a function of impact parameter R from the f/g quasar in SDSSJ0841+3921 , with Poisson error bars. The red curve shows the predicted overdensity profile, based on our measurement of the giant nebulae-LAE cross-correlation function determined from a sample of eight systems – six HzRGs and two LABs – for which published data was available in the literature. Assuming a power-law form for the cross-correlation $\xi_{\text{cross}} = (r/r_0)^{-\gamma}$, we measure the correlation length $r_0 = 29.3 \pm 4.9 h^{-1}$ Mpc, for a fixed value of $\gamma = 1.5$. The gray shaded region indicates the 1σ error on our measurements based on a bootstrap analysis, where both r_0 and γ are allowed to vary. The solid blue line indicates the overdensity of Lyman break galaxies (LBGs) around radio-quiet quasars based on recent measurements (10), with the dotted blue lines the 1σ error on this measurement. On average, the environment of HzRGs and LABs hosting giant Ly α nebulae is much richer than that of radio-quiet quasars (10), confirming that they indeed reside in protoclusters. SDSSJ0841+3921 exhibits a dramatic excess of LAEs compared to the expected overdensities around radio-quiet quasars (blue curve). Its overdensity even exceeds the average protocluster (red curve) by a factor of $\gtrsim 20$ for $R < 200$ kpc decreasing to an excess of ~ 3 on scales of $R \simeq 1$ Mpc, and exhibits a much steeper profile.

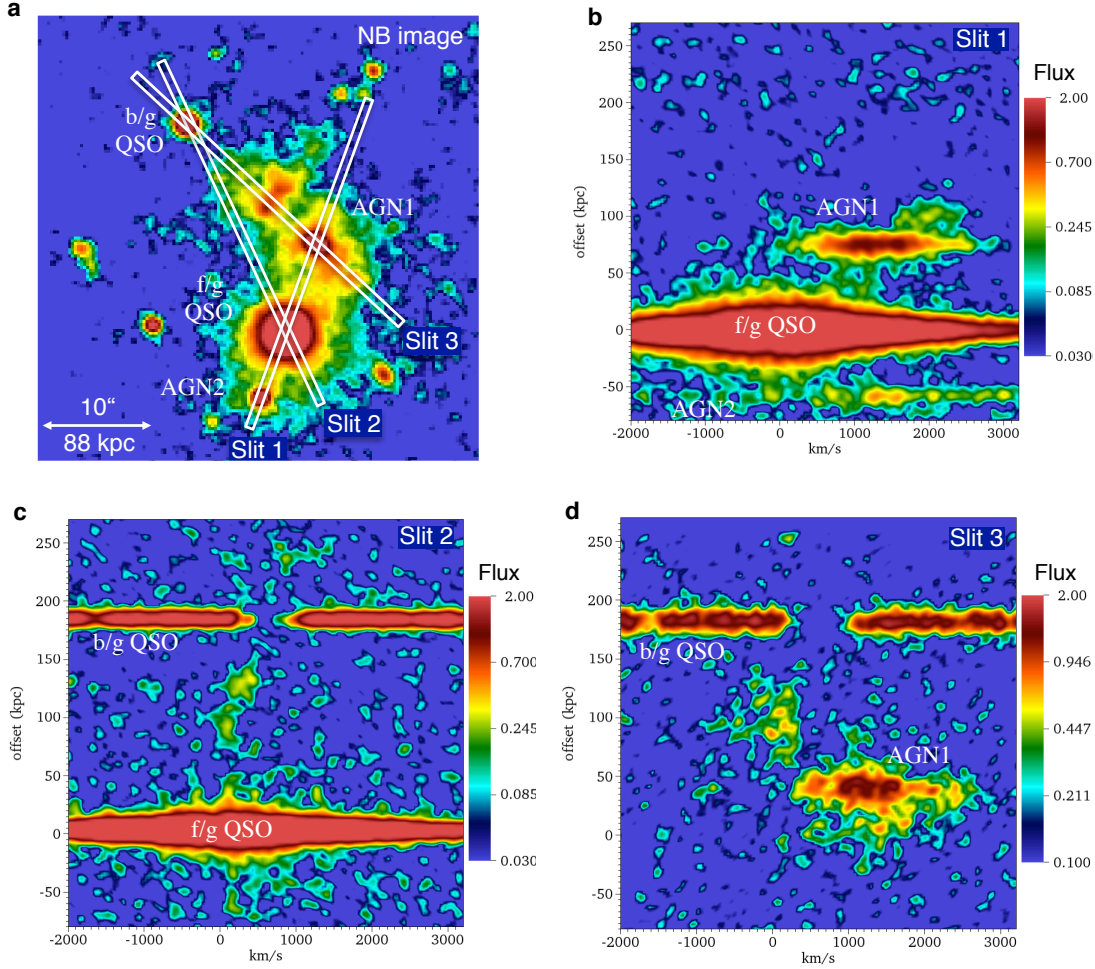


Fig. 3: $\text{Ly}\alpha$ spectroscopy of the giant nebula and its associated AGN. Upper Left: The spectroscopic slit locations (white rectangles) for three different slit orientations are overlayed on the narrow band image of the giant nebula. The locations of the f/g quasar (brightest source), b/g quasar, AGN1, and AGN2 are also indicated. Two-dimensional spectra for Slit1 (**Upper Right**), Slit2 (**Lower Left**), and Slit3 (**Lower Right**) are shown in the accompanying panels. In the upper right and lower left panels, spatial coordinates refer to the relative offset along the slit with respect to the f/g quasar. Spectra of AGN1 are present both in Slit 1 (upper right) and Slit 3 (lower right) at spatial offsets 75kpc and 25kpc, respectively, while the $\text{Ly}\alpha$ spectrum of AGN2 is located at a spatial offset -60 kpc in Slit 1 (upper right). The b/g quasar spectra are located in both Slit 2 (lower left) and Slit 3 (lower right) at the same spatial offset of 176 kpc. The spectroscopic observations demonstrate the extreme kinematics of the system: AGN1 has a velocity of $+1300 \pm 400 \text{ km s}^{-1}$ relative to the f/g quasar and the $\text{Ly}\alpha$ emission in the nebula exhibits motions ranging from -800 km s^{-1} (at ≈ 100 kpc offset in Slit 3, lower right) to $+2500 \text{ km s}^{-1}$ (at ≈ 100 kpc in Slit 1, upper right). A 3×3 pixel boxcar smoothing, which corresponds $120 \text{ km s}^{-1} \times 0.8''$, has been applied to the spectra. In each two-dimensional spectrum, the zero velocity corresponds to the systemic redshift of the f/g quasar. The color bars indicate the flux levels in units of $\text{erg s}^{-1} \text{ cm}^{-2} \text{ arcsec}^{-2} \text{ \AA}^{-1}$.

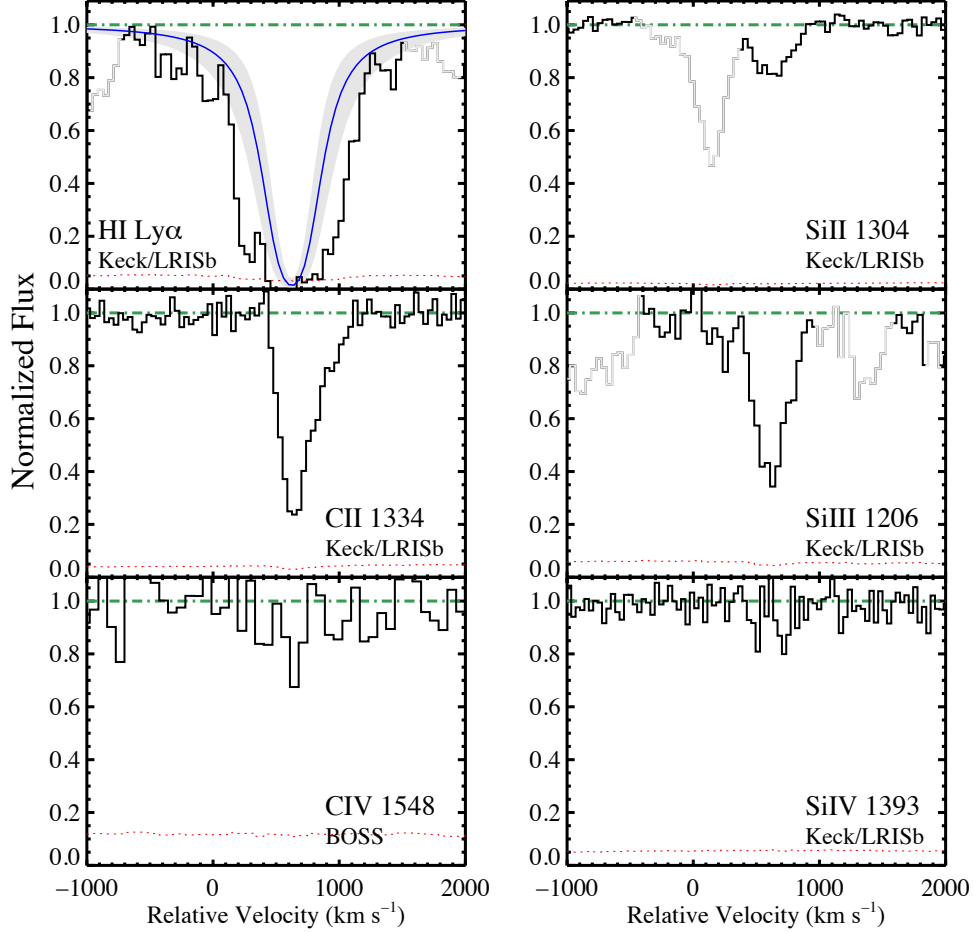


Fig. 4: Absorption line spectrum of cool gas in SDSSJ0841+3921 . Spectrum of the absorbing gas detected in the b/g quasar sightline at an impact parameter of 176 kpc from the f/g quasar. The gas shows strong H I and low-ionization state metal absorption, offset by $\approx 650 \text{ km s}^{-1}$ from the f/g quasar’s systemic redshift. The C II absorption in particular exhibits a significant tail to velocities as large as $\simeq 1000 \text{ km s}^{-1}$, providing evidence for extreme gas kinematics. We modeled the strong H I Ly α absorption with a Voigt profile (blue curve with grey band indicating uncertainty) and estimate a column density $\log N_{\text{HI}} = 19.2 \pm 0.3$. The strong low and intermediate ion absorption (Si II, C II, Si III) and correspondingly weak high-ion absorption (C IV, Si IV) indicate that the gas is not highly ionized, and our photoionization modeling (45) implies $\log_{10} x_{\text{HI}} = -1.2 \pm 0.3$ or $\log_{10} N_{\text{H}} = 20.4 \pm 0.4$. We estimate a conservative lower-limit on the gas metallicity to be 1/10 of the solar value.

Acknowledgments

We thank the staff of the W.M. Keck Observatory for their support during the installation and testing of our custom-built narrow-band filter. We are grateful to B. Venemans and M. Prescott for providing us with catalogs of LAE positions around giant nebulae in electronic format. We also thank the members of the ENIGMA group (<http://www.mpia-hd.mpg.de/ENIGMA/>) at the Max Planck Institute for Astronomy (MPIA) for helpful discussions. JFH acknowledges generous support from the Alexander von Humboldt foundation in the context of the Sofja Kovalevskaja Award. The Humboldt foundation is funded by the German Federal Ministry for Education and Research. J.X.P. acknowledge support from the National Science Foundation (NSF) grant AST-1010004. The data presented here were obtained at the W.M. Keck Observatory, which is operated as a scientific partnership among the California Institute of Technology, the University of California and NASA. The Observatory was made possible by the financial support of the W.M. Keck Foundation. We acknowledge the cultural role that the summit of Mauna Kea has within the indigenous Hawaiian community. We are most fortunate to have the opportunity to conduct observations from this mountain. The data reported in this paper are available through the Keck Observatory Archive (KOA).

Supplementary Online Material

www.sciencemag.org

Materials and Methods

SOM Text

Figs. S1 to S10

Tables S1 to S6

References (52-133)

Supplementary Online Material

This PDF file includes

Materials and Methods

SOM Text

Figs. S1 to S10

Tables S1 to S6

References (52-133)

1 Optical Observations

1.1 Discovery Spectra

The source SDSSJ084158.47+392121.0 (f/g quasar) was targeted as a quasar by the Sloan Digital Sky Survey (SDSS) through their color-selection algorithms and observed spectroscopically in the standard survey (52). It has a cataloged emission redshift of $z = 2.046$. Our analysis of the SDSS imaging data revealed a second, neighboring source at SDSSJ084159.26+392140.0 (b/g quasar) with colors characteristic of a $z \sim 2$ quasar, characterizing this system as a candidate quasar pair. In the course of our ongoing spectroscopic campaign to discover close quasar pairs at $z > 2$ (6, 53), we confirmed this source to have $z = 2.214$ implying a projected quasar pair with a physical separation of $R_{\perp} = 176$ kpc at the f/g quasar redshift. SDSSJ084159.26+392140.0 was also observed by the SDSS-III survey in the Baryonic Oscillating Spectroscopic Survey campaign at a spectral resolution of $R \approx 2000$ and with wavelength coverage $\lambda \approx 3600 - 10,000 \text{ \AA}$ (54).

On UT 2007 Jan 18, we observed the quasar pair with the Low Resolution Imaging Spectrograph (LRIS) (55). These data were taken to study the intergalactic medium probed by the quasar pair, to examine the HI gas associated with the circumgalactic medium of the f/g quasar, and to search for fluorescent emission associated with the f/g quasar. The latter analyses of these data have been presented in previous works (22, 26–28). Summarizing the observations, we used LRIS in multi-slit mode with a custom designed slitmask which allowed placement of one slit on the known quasars and other slits on additional quasar candidates in the field. Specifically, a slit was placed at the position angle $\text{PA}=25.8^{\circ}$ between the f/g and b/g quasars, allowing them to be observed simultaneously. LRIS is a double spectrograph with two arms giving simultaneous coverage of the near-UV and optical. We used the D460 dichroic with the 1200 lines mm^{-1} grism blazed at 3400 \AA on the blue side, resulting in wavelength coverage of $\approx 3250 - 4300 \text{ \AA}$. The dispersion of this grism is 0.50 \AA per pixel and our $1''$ slits give a resolution with full width at half maximum (FWHM) $\text{FWHM} \approx 160 \text{ km s}^{-1}$. On the red side we used the R1200/5000 (covering $\approx 4700 - 6000 \text{ \AA}$) and R300/5000 (covering $\approx 4700 - 10,000 \text{ \AA}$) gratings having a FWHM of $\approx 100 \text{ km s}^{-1}$ and $\approx 400 \text{ km s}^{-1}$ respectively.

The science frames were complemented by a series of calibration images: arc lamp, dome flat, twilight sky, and standard star spectra with the same instrument configurations. All of these exposures were reduced using the LowRedux (<http://www.ucolick.org/~xavier/LowRedux/>) pipeline which bias subtracts and flat fields the images, corrects for non-uniform illumination, derives a wavelength solution, performs sky subtraction, optimally extracts the sources, and fluxes the resultant spectra. The 1D spectra are corrected for instrument flexure and shifted to a heliocentric, vacuum-corrected system.

Using custom software, we also coadded the 2D spectral images to search for diffuse Ly α emission surrounding the f/g quasar (22). This software enables us to model and subtract the spectral PSF of sources in the 2D spectra. Extended Ly α emission will be manifest as residual flux in our 2D sky-and-PSF-subtracted images which is inconsistent with being noise. To visually assess the statistical significance of any putative emission feature, we define a χ image $\chi_{\text{sky+PSF}} = (\text{DATA} - \text{SKY} - \text{OBJECTS})/\sigma$. If our model is an accurate description of the data, the distribution of pixel values in the $\chi_{\text{sky+PSF}}$ should be a Gaussian with unit variance. The middle row of the images in Fig. S1 shows this quantity for SDSSJ 0841+3921 for each slit orientation. The lower row of these images shows $\chi_{\text{sky}} = (\text{DATA} - \text{SKY})/\sigma$. The upper row shows a smoothed version of the middle row, helpful for identifying extended emission. Specifically, the smoothed images are given by $\chi_{\text{smth}} = \frac{\text{CONVOL}[\text{DATA} - \text{SKY} - \text{OBJECTS}]}{\sqrt{\text{CONVOL}^2[\sigma^2]}}$, where the CONVOL operation denotes smoothing of the stacked images with a symmetric Gaussian kernel (same spatial and spectral widths) with FWHM=235 km s $^{-1}$ (dispersion $\sigma_{\text{smth}} = 100 \text{ km s}^{-1}$), which is 5.7 pixels, or 1.4 times the spectral resolution element, and corresponds to FWHM = 1.5'' spatially. The operation CONVOL 2 represents convolution with the square of the smoothing kernel. With this definition of χ_{smth} the distribution of the pixel values in the smoothed image will still obey Gaussian statistics, although they are of course correlated, and hence not independent.

Sky and object PSF-subtracted χ -maps for all of the slit-orientations that we used to characterize extended emission in SDSSJ 0841+3921 are shown in Fig. S1. Fig. 3 of the Main text, shows just the smoothed sky-subtracted images with a color-map chosen to accentuate the faint extended emission and a slightly different smoothing, namely a 3×3 pixel boxcar smoothing, which corresponds $120 \text{ km s}^{-1} \times 0.8''$. The χ -maps in Fig. S1 enable the reader to objectively assess the statistical significance of all emission features in the unsmoothed data. Note that in all of these maps, only the PSF model of the f/g and b/g quasars have been subtracted, whereas neither AGN1 nor AGN2 were removed from the other slit-orientations (see Fig. 1 in main text). Following the calibration procedure described in (22), we deduce the following spectroscopic surface brightness limits (1σ) for the Ly α line at the f/g quasar redshift $z = 2.0412$: Slit1, $\text{SB}_{1\sigma} = 2.2 \times 10^{-18} \text{ erg s}^{-1} \text{ cm}^{-2} \text{ arcsec}^{-2}$; Slit2, $\text{SB}_{1\sigma} = 2.3 \times 10^{-18} \text{ erg s}^{-1} \text{ cm}^{-2} \text{ arcsec}^{-2}$; and Slit3, $\text{SB}_{1\sigma} = 4.8 \times 10^{-18} \text{ erg s}^{-1} \text{ cm}^{-2} \text{ arcsec}^{-2}$, where these SBs are computed in windows of $700 \text{ km s}^{-1} \times 1.0''$, which corresponds to an aperture of $700 \text{ km s}^{-1} \times 1.0 \text{ arcsec}^2$ on the sky because we always used a 1.0'' slit. The depth that we attain in our Ly α spectroscopy is comparable to that achieved by our narrow-band imaging $\text{SB}_{1\sigma} = 1.7 \times 10^{-18} \text{ erg s}^{-1} \text{ cm}^{-2} \text{ arcsec}^{-2}$ (see next section).

The original observation from the Quasars Probing Quasars (QPQ) (22) survey corresponds to slit-orientation Slit2 (see Fig. S1 and Fig. 3 in main text). Our initial visual inspection of the Ly α emission map revealed a bridge of Ly α emission along the slit connecting the quasar pair. Although the SB varies with position, this structure has a characteristic $SB_{Ly\alpha} \simeq 10^{-17} \text{ erg s}^{-1} \text{ cm}^{-2} \text{ arcsec}^{-2}$ and is detected at $\simeq 4 - 5\sigma$ at location $R_{\perp} \simeq +100 \text{ kpc}$ between the two quasars. The emission extends along the slit from -80 kpc below the f/g quasar to $+150 \text{ kpc}$ between the two quasars, and possibly to $+250 \text{ kpc}$. With an end-to-end size of $\sim 250 \text{ kpc}$, this represented one of the largest Ly α emission nebula ever detected, and thus motivated the additional imaging and spectroscopic observations, which are the focus of this manuscript.

1.2 Narrow Band Imaging

We purchased a custom-designed narrow-band (NB) filter from Andover Corporation, sized to fit within the grism holder of the Keck/LRISb camera. The filter was tuned to $\lambda_{\text{center}} = 3700\text{\AA}$, and designed with a narrow band-pass $\text{FWHM}_{\lambda} = 33\text{\AA}$ to minimize sky background while maintaining throughput. On UT 12 November 2012, we imaged the $\sim 5' \times 7'$ field-of-view surrounding SDSSJ0841+3921, offset to place the quasar pair on the CCD with highest quantum efficiency. We observed for a total of 3.2 hours in a series of dithered, 1280s exposures. Conditions were clear with sub-arcsecond atmospheric seeing. In parallel, we obtained 3hrs of broad-band V images with the LRISr camera. The instrument was configured with the D460 dichroic and the detectors of the blue camera were binned 2x2 to minimize read noise.

The images were reduced using standard routines within the IRAF reduction software package. This includes bias subtraction, flat fielding and an illumination correction. A combination of twilight sky flats and unregistered science frames were used to produce flat-field images and illumination corrections in each band. The individual frames were sequentially registered to the SDSS-DR7 catalog using the SExtractor (56) and SCAMP (57) packages. The RMS uncertainty in the astrometry of our registered images is approximately $0.2''$. Finally, the corrected frames from each band were average-combined using the SWarp package (58).

We calibrated the photometry of our images as follows. At the beginning and end of the night, we observed two spectrophotometric stars (G191b2b and Feige34) with the NB filter under clear conditions. Neither star has significant spectral features in the relevant wavelength range covered by our NB filter. For the broad-band images, we observed the standard star field PG0231+051. To compute the zero-point for the narrow-band images, we compared the measured count rates of Feige34 and G191b2b with the expected fluxes estimated by convolving the standard star spectra (resolution of 1\AA) (59) with the normalized filter transmission curve. We calculate an average, zero-point magnitude of 23.58 mag, with a few percent difference between the two stars. With this calibration, we deduce that the 1σ limiting surface brightness of our combined NB images is $SB_{1\sigma} = 1.7 \times 10^{-18} \text{ erg s}^{-1} \text{ cm}^{-2} \text{ arcsec}^{-2}$ for a 1.0 arcsec^2 aperture.

For the broad-band images, we compared the number of counts per second of the five stars in

the PG0231+051-field with their tabulated V -band magnitudes (60). The derived zero-point for the five stars are consistent to within a few percent and we adopt the average value: $V_{\text{ZP}} = 28.07$. Because the Feige34 and the PG0231+051 fields were observed with an airmass ($\text{AM} \approx 1.2$) similar to our science field, we did not correct the individual images before combination. We estimate that the correction would be on the order of few percent. The 1σ limiting point source magnitude for our combined broad band images is $V = XX$.

To isolate the emission in the $\text{Ly}\alpha$ line we estimated and then subtracted the continuum emission underlying the NB3700 filter. We estimate the continuum using the V -band (not affected by the $\text{Ly}\alpha$ line) and assuming a flat continuum slope (in frequency), i.e. $\beta_\lambda = -2$. This assumption is dictated by our dataset, i.e. we can rely only on a deep V -band image to estimate the continuum, and it follows the prescriptions of previous work (61) which showed that $\beta_\lambda \sim -1.9$ for the most luminous sources and higher values for the faintest. Thus, assuming a flat continuum slope gives us a conservative estimate of the $\text{Ly}\alpha$ emission and its equivalent width. As the V -band image has slightly worse seeing ($\sim 1.3''$), we convolved the NB image to the same seeing before subtracting the continuum. The continuum subtraction has been applied using the following formula

$$\text{Ly}\alpha = \text{NB3700} - \frac{\text{FWHM}_{\text{NB3700}}}{\text{FWHM}_V} \frac{\text{Tr}_{\text{NB3700}}}{\text{Tr}_V} V, \quad (1)$$

where $\text{Ly}\alpha$ is the final subtracted image, NB3700 is the narrow-band image, V is the V -band image, and $\text{Tr}_{\text{NB3700}}$ and Tr_V are the peak transmission values for the NB3700 and V -band filters, respectively. The result of this procedure is a $\text{Ly}\alpha$ only narrow-band image, which is shown in the left panel of Fig. 1.

1.3 Follow-up Spectroscopy

After the discovery of an extended nebula in our NB imaging, we opted to obtain additional spectroscopy of both the diffuse nebula and several compact sources near the projected quasar pair during the same observing run. On UT 13 November 2012 in clear observing conditions and seeing varying from $\text{FWHM} = 0.6 - 1.0''$, we used the LRIS spectrometer with a $1.0''$ longslit, configured with the D460 dichroic, B1200/3400 grism, and R600/7500 grating. We obtained two additional orientations of the longslit as illustrated in Fig. 3: (Slit 1) along the line connecting source f/g quasar and AGN2 with a $\text{PA}=227^\circ$; (Slit 3) along the line connecting the b/g quasar and AGN1 with a $\text{PA}=343^\circ$. We exposed for a total of 4800s and 2400s for Slit 1 and Slit 3, respectively. The PA of Slit 1 was chosen to be aligned with the f/g quasar and a nearby radio source detected in the FIRST survey (see Supp. 2.2), which we learned about just prior to the November 2012 Keck observations. This turned out to be an AGN at the same redshift (AGN2). The slit orientation also conveniently allowed us to simultaneously observe a bright spot in the $\text{Ly}\alpha$ image, which is also the companion AGN1. The orientation of Slit 3 was chosen to be aligned with the b/g quasar as a position reference and two other bright spots in the nebula, one of which was also covered by Slit 1, i.e. AGN1. Coordinates, photometry, and

other information about these targets are listed in Table S1. Corresponding calibration frames were obtained and these data were reduced with the same procedures described above. The slit orientation of our original January 2007 spectroscopy is also indicated in Fig. 3 as Slit 2, which simultaneously observed the f/g and b/g quasars at PA=25.8° for an exposure time of 1800s (but in better conditions).

Our Ly α image (left panel of Fig. 1) reveals several compact Ly α -emitting sources (LAEs) with rest-frame $W_{\text{Ly}\alpha} > 20\text{\AA}$ in the vicinity of the f/g quasar, which are hence very likely to be at the same redshift. On UT 2012 Dec 14, we targeted two of these LAEs with the DEIMOS spectrometer (62) on the Keck II telescope in partly cloudy conditions. Specifically, we employed the 1.0'' long-slit mask oriented to cover the object labeled AGN3 in Fig. 1 (see also Table S1), and another LAE which we designate as Target1 at RA=08:41:58.8, DEC= +39:21:57.4, which lies off of the image in Fig. 3. The instrument was configured with the 600ZD grating tilted to a central wavelength of 7200Å which provides coverage from $\approx 4600 - 9800\text{\AA}$ with a spectral resolution FWHM $\approx 235\text{km s}^{-1}$. We took two exposures totaling 4500s. These data were reduced and extracted with the SPEC2D pipeline (63, 64) and fluxed using a spectrum of the spectrophotometric standard star Feige 34 taken that (non-photometric) night with the same instrument configuration. Note that given the limited blue sensitivity of DEIMOS, these spectra did not cover the Ly α emission line at $\simeq 3700\text{\AA}$. Owing to its faint continuum magnitude ($V = 25.2\text{ mag}$) the spectrum of Target1 was inconclusive, although its large Ly α equivalent width $W_{\text{Ly}\alpha} = 97\text{\AA}$ suggests it is a real LAE. A setup covering Ly α is likely necessary to spectroscopically confirm this source. The object AGN3 is an AGN at the same redshift as the f/g quasar, as described in the next section.

2 Discovery of Four AGN

Our follow-up spectroscopy reveals three additional AGN within $\theta < 18''$ or $R_{\perp} < 150\text{ kpc}$ of the f/g quasar, with very similar redshifts. These objects are labeled as AGN1-3 in Fig. 3, and their optical spectra are shown in Fig. S2. Relevant information for all five of the AGN associated with the nebula, namely the f/g quasar, the three AGN discovered at the same redshift, and the b/g quasar are provided in Table S1.

Motivated by the discovery of these AGN, we force-photometered the SDSS and WISE survey images at the coordinates of each AGN, measured from our deep Keck images. This was performed using a custom algorithm (65), which simultaneously models the input sources at their respective locations, as well as all other nearby sources detected in the SDSS survey imaging. This modeling fully accounts for the potentially overlapping PSFs of the sources (a significant issue for WISE given its FWHM $\approx 6''$ PSF), and thus effectively de-blends the photometry. It also utilizes data from multiple visits, thus effectively co-adding all epochs and improving the effective depth over that in the published catalogs. Table S2 shows photometry for the five AGN. There we list the SDSS *ugriz* and WISE *W1, W2, W3, W4* measurements determined from our forced photometry procedure, measurements or limits on the Peak 20cm

radio flux $F_{20\text{cm}}$ from the FIRST survey, the LRIS V -band photometry, the $\text{Ly}\alpha$ line-flux, and the rest-frame $\text{Ly}\alpha$ equivalent width.

2.1 AGN1: An Obscured Type-2 Quasar

The object AGN1 is embedded in a bright ridge of the nebular $\text{Ly}\alpha$ emission, as shown in our $\text{Ly}\alpha$ image and the 2D spectrum (Fig. 3). Our LRIS spectra have relatively low continuum signal-to-noise $S/N \sim 1 - 2$ ratio, consistent with the faint continuum magnitude of AGN1: $V = 23.95 \pm 0.07$. Nevertheless, we detect strong emission in several lines: $\text{He II}\lambda 1640$, $\text{C III}\lambda 1908$, $\text{C II}\lambda 2328$, and a tentative detection of $\text{C IV}\lambda 1549$, along with bright $\text{Ly}\alpha$, which our narrow-band imaging indicated should be strong. The FWHM, line flux, and rest-frame equivalent widths (EWs) of these lines are listed in Table S3. The presence of emission in several high-ionization UV lines (i.e. He II and C IV) characteristic of AGN, clearly indicates that this source is powered by a hard-ionizing spectrum, rather than star-formation. Although high-ionization lines like C IV , He II , and C III can be formed in starbursts, stellar winds, the photospheres of massive stars, and the interstellar medium, the spectra of star-forming galaxies typically exhibit much smaller rest-frame EWs ($\lesssim 2\text{\AA}$) (66) in these lines than observed in our spectra. Several independent lines of argument suggest that this object is actually a luminous but obscured quasar, also referred to as a Type-2 quasar, as we elaborate on below. From the weak $\text{He II}\lambda 1640$ line, we measure $z = 2.05476$ which is $\approx 300\text{km s}^{-1}$ lower than the estimates from $\text{Ly}\alpha$, and $\text{C III}\lambda 1908$. We estimate an uncertainty in this redshift of 400km s^{-1} , which arises both because of line-centroiding error, and possible systematic uncertainty about the degree to which a high-ionization line like $\text{He II}\lambda 1640$ traces the systemic frame for a Type-2 AGN.

According to unified models of AGN (67, 68), orientation is the primary determining factor governing the ultraviolet/optical appearance of an AGN. In this context, vantage points which are not extinguished by the obscuring torus observe a spatially unresolved power-law ultraviolet and optical continuum believed to emerge from the SMBH accretion disk, and broad high-ionization emission lines ($\text{FWHM} \simeq 5000 - 20,000\text{km s}^{-1}$) from photoionized gas in the so called broad line region at distances $\sim 1\text{pc}$ from the SMBH. However, all vantage points, observe narrow emission lines from the spatially extended ($\sim 100\text{pc} - 10\text{kpc}$) narrow ($\text{FWHM} \simeq 500 - 1500\text{km s}^{-1}$) line region. When the line-of-sight to the central engine is blocked by a dusty obscuring torus, only the narrow line region is seen. AGN lacking broad emission lines, but which nevertheless exhibit narrow high-ionization lines are classified as Type-2 systems, while those with broad-line emission are classified as Type-1. Alternatives to the AGN unification viewing angle picture argue instead that Type-1s and Type-2s represent different phases of quasar evolution (69), with all quasars passing through an obscured phase before outflows expel the obscuring material.

Characteristics of Type-2 quasars at other wavelengths are a hardened X-ray spectrum, resulting from photoelectric absorption of soft X-rays presumably from the same obscuring torus extinguishing the broad-line region, and strong mid-IR ($\lambda \sim 10\text{ }\mu\text{m}$) emission, which represents ultraviolet/optical energy emitted from the disk, but absorbed, reprocessed, and re-emitted

isotropically by the torus. In a subset of radio-loud systems, synchrotron radiation, believed to be emitted isotropically from scales much larger than the torus, is also observed.

Luminous high-redshift radio-loud Type-2 quasars have been studied for decades (see the review by (70)) but their radio-quiet counterparts have been much harder to identify. Over the past decade, significant progress has been made in identifying sizable samples of low-redshift ($z \lesssim 1$) radio-quiet Type-2s from mid-IR (71, 72), X-ray (73), and optical narrow-line emission (74). However, to date the vast majority of these Type-2s are at $z < 1$, and there are still only handfuls of bonafied Type-2 quasars known at $z \sim 2$ (75) with bolometric luminosities comparable to the typical SDSS/BOSS Type-1 quasar, $L_{\text{bol}} \gtrsim 10^{46} \text{ erg s}^{-1}$.

The three lines of argument that we use to establish that AGN1 is a Type-2 quasar are 1) the narrow velocity width of its emission lines 2) the line ratios in its spectrum, and 3) its extremely red optical-to-mid-IR colors.

Unlike the three other AGN physically associated with the nebula (f/g quasar, AGN2, and AGN3), which exhibit broad emission lines ($\text{FWHM} \simeq 5000 - 10,000 \text{ km s}^{-1}$), Gaussian fits to the lines in AGN1 reveal relatively narrow lines $\lesssim 1500 \text{ km s}^{-1}$, which are listed in Table S3. At low-redshifts ($z < 0.3$), AGN exhibit a bimodal distribution of $\text{H}\alpha$ emission line widths, which corresponds to the Type-1 and Type2 populations. Based on this distribution, the canonical dividing line between Type-1/Type-2 quasar classification is $\text{FWHM}_{\text{H}\alpha} < 1200 \text{ km s}^{-1}$ (76). However, it is unclear how to extrapolate this classification to the rest-frame UV lines observed at $z \sim 2$. First, higher redshift sources are intrinsically much more luminous, have more massive SMBHs, and hence SMBH-galaxy scaling relations imply that they should be hosted by much more massive galaxies. Indeed, for the handful of Type-1 quasars at $z \sim 2$ for which the narrow-line region [O III] emission line has been observed in the near-IR, larger line-widths $\text{FWHM} = 1300 - 2100 \text{ km s}^{-1}$ are indeed observed (77), contrasting with narrower line widths observed at lower redshift (76). Furthermore, even in the narrow-line region, one generally expects larger widths for $\text{Ly}\alpha$ and higher ionization potential lines, because photoionization modeling generally predicts that emission in these lines is produced at smaller distances from the nucleus, where velocities are likely to be larger. Indeed, exactly such trends were observed in the spectrum of a Type-2 quasar at $z = 3.288$ discovered by (78), who measured $\text{FWHM}_{\text{Ly}\alpha} = 1520 \pm 30 \text{ km s}^{-1}$, $\text{FWHM}_{\text{HeII}} = 940 \pm 140 \text{ km s}^{-1}$, and $\text{FWHM}_{\text{CIII]]}} = 1090 \pm 140 \text{ km s}^{-1}$, which are comparable to our measured values for AGN1. A near-IR spectrum of the Stern et al. source reveals narrower widths for the rest-frame optical lines that are typically used to classify low-redshift Type-2s: $\text{FWHM}_{\text{H}\beta} = 170 \pm 130 \text{ km s}^{-1}$ and $\text{FWHM}_{\text{[OIII]}} = 430 \pm 30 \text{ km s}^{-1}$. Note that the unusually hard X-ray spectrum of the Stern et al. source (78) and the implied high photoelectric absorbing column $N_{\text{H}} = (4.8 \pm 2.1) \times 10^{23} \text{ cm}^2$ leave little doubt that it is a bonafied Type-2 quasar, notwithstanding the fact that $\text{Ly}\alpha$ and other high-ionization UV lines have line widths in excess of $\text{FWHM} = 1200 \text{ km s}^{-1}$. We suspect that the canonical rest-frame optical line-width classification based on $z < 0.3$ Type-2 quasars (76) needs to be revised for rest-frame UV lines in more luminous Type-2s at $z \sim 2$. Based on the narrow lines of AGN1 and their similarity to the Stern et al. source (78), we conclude that it is very likely to be a Type-2 quasar.

Table S3 presents measurements of the line fluxes and measurements or limits on rest-frame equivalent width for the characteristic AGN lines covered by our spectrum. Based on these line flux measurements, Fig. S3 shows the line-ratios of AGN1 in the C IV/He II vs C IV/C III] plane (left) as well as the C III]/He II vs C III]/C II] plane (right). These are the standard line ratios conventionally discussed in studies that use photoionization modeling to diagnose the physical conditions in the narrow-line region (79), although we note that the ratios C III]/He II vs C III]/C II] are not typically plotted against each other. In Fig. S3, we compare the line ratios of AGN1 to other Type-2 AGN compiled from the literature. Specifically, the circles are individual measurements of HzRGs (black) from the compilation of (80), and narrow-line X-ray sources (cyan) and Seyfert-2s (blue) from the compilation of (81). In addition, triangles indicate measurements from the composite spectra of HzRGs (orange) from (70), the composite Type-2 AGN spectra (purple) from (82), who split their population into two samples above and below Ly α EW of 63Å, and a composite spectrum of mid-IR selected Type-2 AGN (green) from (83). Finally, the stars represent measurements of these line ratios from composite spectra of Type-1 quasars, based on the analysis of (magenta) (84), (red-magenta) (85), and (blue-magenta) (86).

We caution that determination of robust emission line fluxes for Type-1 quasars is extremely challenging. Generally the broad emission lines, non-trivial emission line shapes, and the fact that many of the lines of interest are severely blended, makes the separation of the spectrum into line and continuum rather ambiguous. To minimize the impact of noise and variations among quasars, one typically analyzes extremely high signal-to-noise ratio composite spectra, which also average down quasar-to-quasar variation (84–86). But nevertheless, the resulting line fluxes and hence line flux ratios are dependent on the method adopted (see (85)) section 4.1 for a detailed discussion). These issues are particularly acute for the lines that we consider: He II λ 1640 is heavily blended with the red wing of C IV λ 1549 and O III] λ 1663, Al II λ 1670, and a broad Fe II complex, C III] λ 1909 is severely blended with Al II λ 1857 and Si III λ 1892, and C II] λ 2326 is blended with a broad Fe II complex. These ambiguities are reflected in the large variation in the line ratios determined from Type-1 quasar composites in Fig. S3 (stars) by different studies. Despite these challenges, Fig. S3 clearly illustrates that the line-ratios for AGN1 are consistent with the Type-2/Seyfert-2 locus, and differ rather significantly from the Type-1 line ratios, notwithstanding the somewhat divergent measurements for the latter. We thus conclude based on the emission line ratios of AGN1 that it is very likely to be a Type-2 AGN.

Many studies utilizing WISE data have shown that at bright magnitudes $W2 \simeq 15$ mag, the WISE $W1 - W2$ color efficiently selects AGN at $z \sim 1 - 3$, including obscured objects (87–89). This results from the rising roughly power law shape of AGN SEDs in the mid-IR (90, 91), and the fact that stellar contamination is low, because the WISE $W1$ and $W2$ bands cover the Rayleigh-Jeans tail of emission from Galactic stars, resulting in much bluer colors which cleanly separate from redder AGN. At fainter magnitudes $W2 \simeq 17$, contamination increases because of optically faint, high-redshift elliptical and Sbc galaxies, which tend to also have very red $W1 - W2$ colors. In addition, obscured AGN are also expected to have very red optical to mid-IR colors, if the mid-IR traces reprocessed dust emission from a heavily

extincted accretion disk emitting in the optical/UV. Indeed, it has been shown that the color-cut $r - W2 > 6$ effectively separates obscured AGN from their much bluer unobscured counterparts (89, 92, 93). The WISE photometry in Table S2 indicate that AGN1 is detected in both $W1$ and $W2$ with $W1 = 16.89 \pm 0.08$, and $W2 = 15.86 \pm 0.11$, implying a $W1 - W2 = 1.03 \pm 0.14$, thus consistent with the expected red color $W1 - W2 > 0.8$ of AGN in the WISE bands. If we adopt our LRIS V-band magnitude as a proxy for r (color corrections are minimal), then the faint $V = 23.95$ continuum of AGN1 implies $r - W2 = 8.09 \pm 0.13$, which is also consistent with the $r - W2 > 6$ criterion for obscured AGN. We thus conclude based on mid-IR and mid-IR to optical colors, that AGN1 is consistent with being an obscured AGN.

2.2 AGN2: A Radio Loud Broad Line AGN

The second quasar (AGN2) is rather faint $V = 23.12$ (Table S1), but its LRIS spectrum nevertheless reveals broad $\text{Ly}\alpha$, $\text{C IV } \lambda 1549$, and $\text{C III } \lambda 1909$ emission lines, unequivocally indicating that it is a broad-line Type-1 AGN (see Fig. S2). Centroiding the broad and relatively low S/N $\text{C III } \lambda 1908$ line, we estimate $z_{\text{AGN2}} = 2.058$ with a 700 km s^{-1} uncertainty. Redshift errors for rest-frame ultraviolet emission lines are dominated by intrinsic shifts between the emission line and the true systemic frame, and we adopt the procedure described in (23) to centroid the broad lines, and use the procedure of (94) to determine the redshift errors.

Motivated, in part, by the previous association of bright $\text{Ly}\alpha$ nebulae to HzRGs and/or bright radio sources, we searched the literature and public catalogs for sources in the field surrounding SDSSJ0841+3921. The Faint Images of the Radio Sky at Twenty cm survey (FIRST) (95) used the Very Large Array (VLA) to produce a map of the 20 cm (1.4 GHz) sky with a beam size of $5.''4$ and an RMS sensitivity of about $0.15 \text{ mJy beam}^{-1}$. The survey covers the same $10,000 \text{ deg}^2$ sky region covered by the SDSS imaging, has a typical detection threshold of 1 mJy , and an astrometric accuracy of $0.05''$. The FIRST catalog reports only a single source within $60''$ of SDSSJ0841+3921 at RA=08:41:58.6 DEC=+39:21:14.7, approximately $6''$ South of the f/g quasar and coincident with AGN2. The FIRST peak and integrated fluxes at 20 cm are $F_{\text{peak}} = 12.87 \text{ mJy/beam}$ and $F_{\text{int}} = 14.81 \text{ mJy}$ respectively, giving a morphological parameter $\Theta = \log_{10}(F_{\text{int}}/F_{\text{peak}}) = 0.06$. This indicates a compact, unresolved source at 1.4 GHz (96). Therefore, there is no evidence for a bright, extended radio source (e.g. a radio jet) associated with the protocluster system and giant $\text{Ly}\alpha$ nebula.

Follow-up VLA observations of this source were performed by (97), having erroneously associated it with the f/g quasar. The spectral slope measured from 8.4 GHz and 4.9 GHz observations is relatively steep, $\alpha_{4.9}^{8.4} = -1.21$, which is generally interpreted as evidence that the source has a large viewing angle (i.e. edge-on) (98). This may indicate that FIRSTJ084158.6+392114.7 (AGN2) is oriented away from us, although we re-emphasize that it exhibits a Type-1 spectrum. These much deeper radio images of the source show no evidence for extended structure or jets, providing further evidence that it is not a HzRG (97).

2.3 AGN3: A Faint Broad Line AGN

Similar to AGN2, the source AGN3 is also faint $V = 23.09$ but exhibits broad emission-lines of $\text{C IV } \lambda 1549$, $\text{C III] } \lambda 1908$, and $\text{Mg II } \lambda 2798$ (see Fig. S2). Unfortunately $\text{Ly}\alpha$ was not covered by our DEIMOS spectrum, but the source has a large rest-frame equivalent width ($W_{\text{Ly}\alpha} = 35\text{\AA}$) indicative of strong emission. Based on the broad lines, we also classify this source as a broad-line (Type-1) AGN. We determine a redshift of $z_{\text{AGN3}} = 2.050$ from the $\text{C III] } \lambda 1908$ line with a 700 km s^{-1} uncertainty.

3 Probability of Finding a Quadruple Quasar

The probability dP of detecting three quasars around a single known quasar (here the f/g quasar) can be written as

$$\begin{aligned} dP = & n_{\text{QSO}}^3 dV_2 dV_3 dV_4 [1 \\ & + \xi(r_{12}) + \dots \quad (6 \text{ permutations}) \\ & + \zeta(r_{12}, r_{23}, r_{31}) + \dots \quad (4 \text{ permutations}) \\ & + \xi(r_{12})\xi(r_{34}) + \dots \quad (3 \text{ permutations}) \\ & + \eta(r_1, r_2, r_3, r_4)] \end{aligned} \quad (2)$$

where n_{QSO} is the number density of quasars, dV_i is the infinitesimal volume element centered on the location \vec{r}_i of the i th quasar, r_{ij} is the distance between the i th and j th quasar, and ξ , ζ , and η are the two-point, three-point, and four-point correlation functions, respectively (99).

The total probability P of finding a quadruple quasar system within a maximum radius r_{max} is the integral $\int dP$ over the three volume elements dV_i , for all possible configurations of the \vec{r}_i . Our goal in what follows is to obtain an order of magnitude estimate for this total probability.

First note that on the small scales of interest to us (here $r \lesssim 200\text{ kpc}$), many of the terms in eqn. (2) can be neglected. For the higher order correlation functions ζ and η , a scaling of the form $\zeta \propto \xi^2$ and $\eta \propto \xi^3$ is often assumed. This arises from the fact that for Gaussian initial conditions and a scale-free initial power spectrum, this scaling is obeyed to second order in Eulerian perturbation theory (100). However, this scaling is not valid for the highly non-linear small-scales of interest to us here. On these small scales, we follow the halo model approach (101), and write the higher order functions as a sum of terms representing contributions from the multiple possible halos. For example the four-point function can be written as the sum

$$\eta = \eta^{1\text{h}} + \eta^{2\text{h}} + \eta^{3\text{h}} + \eta^{4\text{h}}, \quad (3)$$

resulting from contributions from one to four halos. As we are concerned with scales comparable to the virial radius of the dark matter halo hosting, i.e. the f/g quasar $r \lesssim 200\text{ kpc}$, the one halo term, which quantifies the four-point correlations when all four points lie in the same dark matter halo, will dominate (101). It is easier to calculate this one-halo term of the four-point function $\eta^{1\text{h}}$ in Fourier space, where one instead works with the one halo term of the trispectrum $T^{1\text{h}}$, and it can be shown that $T^{1\text{h}}$ scales as the Fourier transform of the dark matter

halo density profile to the fourth power $T^{1h} \propto \rho_{DM}^4$. This scaling holds likewise for η . Thus for quasar 4-point correlations on small-scales, the halo model indicates that we expect $\eta \propto \rho_{QSO}^4$, where ρ_{QSO} is the density profile of quasars in the dark matter halos which host them.

By a similar line of argument, the small-scale two- and three-point functions scale as $\xi \propto \rho_{QSO}^2$ and $\zeta \propto \rho_{QSO}^3$, respectively. Or alternatively, $\zeta \propto \xi^{3/2}$ and $\eta \propto \xi^2$. On the proper scales of interest to us here $r \lesssim 200$ kpc ($r_{com} = 600$ kpc, comoving), $\xi \gg 1$ and thus the terms dominating eqn. (2) are the three permutations of terms like $\xi(r_{12})\xi(r_{34})$, and η , which are all of comparable order ξ^2 .

Thus in order to compute the total probability of finding three quasars around a known quasar, we must integrate the four dominant terms in eqn. (2), over all possible configurations of the \vec{r}_i , which can be realized within a spherical volume, whose radius is set by the largest separation in the quadruple quasar r_{max} . These integrals all have a common form and order-of-magnitude. For example the first three terms involving pairs of correlation functions can be written

$$n_{QSO}^3 \left(\int_0^{r_{max}} \xi(r) 4\pi r^2 dr \right) \left(\int \xi(r_{34}) dV_3 dV_4 \right) \sim n_{QSO}^3 \left(\int_0^{r_{max}} \xi(r) 4\pi r^2 dr \right)^2 V, \quad (4)$$

where $V = 4\pi/3 r_{max}^3$. Thus the final expression for an order-of-magnitude estimate of the probability is

$$P \sim 4n_{QSO}^3 \left(\int_0^{r_{max}} \xi(r) 4\pi r^2 dr \right)^2 V, \quad (5)$$

where the factor of four accounts for the four similar dominant terms of order $\sim \xi^2$ in eqn. (2).

To calculate n_{QSO} , we use the quasar luminosity function of (102) assuming an apparent magnitude limit $V < 24$. This limit is highly conservative, as even AGN2 and AGN3 have $V = 23.1$ mag. Although the Type-2 AGN1 has $V = 24$, its nucleus is obscured from our perspective, and this magnitude represents host-galaxy emission or a small-fraction $\sim 5\%$ of scattered nuclear emission. The corresponding nuclear V -band emission of this AGN is likely to be much brighter than $V = 24$ given that its $Ly\alpha$ flux, coming from the narrow-line region, is so strong, i.e. larger than that of AGN2. To account for the fact that our luminosity function only includes unobscured AGN, we divide it by a factor $(1 - f_{obs})$, where f_{obs} is the obscured fraction of AGN. We adopt an obscured fraction of $f_{obs} = 0.5$ consistent with recent determinations (103, 104). Altogether, we estimate that the comoving number density of faint AGN is $n_{QSO} = 3.8 \times 10^{-5} \text{ cMpc}^{-3}$.

We assume that all four AGN reside in a physical structure with physical size r_{max} . This is a good assumption, given that: the projected separations of the AGN are small, they reside in a larger-scale overdensity of $Ly\alpha$ emitters, the f/g quasar, AGN1, and AGN2 are all embedded in the giant $Ly\alpha$ nebula, and the morphology of the nebular emission around the AGN suggests a physical association. Moreover, although we argue here that the probability of finding a quadruple AGN is very small, it would be much smaller if the AGN had larger line-of-sight separations, in which case one cannot invoke as large of an enhancement due to clustering. Taking the f/g

quasar location as the origin, the largest angular separation measured in the quadruple quasar is that of AGN3 with $\theta = 18''$, corresponding to a transverse separation $r_{\perp} = 150$ kpc. We thus choose $r_{\max} = 250$ kpc, such that the spherical comoving volume we consider corresponds to $V = 1.9 \text{ cMpc}^3$. The probability of finding the three AGN around the f/g quasar at random, i.e. in the absence of clustering, is extremely small $P_{\text{ran}} = (n_{\text{QSO}} V)^3 = 3.4 \times 10^{-13}$.

The small-scale two-point correlation function of quasars was first computed by (6), and later extended to even smaller scales ~ 5 kpc by the gravitational lensing search of (30), who found that a power law form $\xi = (r/r_0)^{-\gamma}$ with $\gamma = -2$ and $r_0 = 5.4 \pm 0.3 h^{-1} \text{ cMpc}$ provides a good fit to the data over a large range of scales. Plugging these numbers into eqn. (5), we finally arrive at a probability of $P = 6.9 \times 10^{-8}$, justifying our order of magnitude estimate of $P \sim 1 \times 10^{-7}$.

4 Giant Nebulae-LAE Clustering Analysis

4.1 Constructing the LAE Catalog

We created an LAE catalog from our images of SDSSJ0841+3921 using *SExtractor* (105) in dual-mode, using the NB image as the reference image. In order to minimize spurious detection we varied the parameters DETECT_MINAREA (minimum detection area) and DETECT_THRESH (relative detection threshold) creating a large number of LAE candidate catalogs. We verify the number of spurious detections for each catalog running *SExtractor* on the “negative” NB image obtained by multiplying the NB image by -1 . The ratio between the number of sources detected in the NB image and the sum of sources detected in both the NB and “negative” image define a “reliability” criterion. We selected DETECT_MINAREA equal to 8 pixels and DETECT_THRESH equal to 1.8σ corresponding to a “reliability” of 94%. We used the same parameters to obtain a catalog of sources for the V -band image. In order to select LAE candidates, we estimated the NB $- V$ color from *SExtractor* isophotal magnitudes and applied a color-cut corresponding to a $\text{Ly}\alpha$ rest-frame equivalent width of $W_{\text{Ly}\alpha} > 20\text{\AA}$ which is the standard threshold used in the literature. In particular, we assumed a flat continuum slope in frequency to convert the V -band magnitude to a continuum flux at the $\text{Ly}\alpha$ wavelength. For the objects in the catalog without broad-band detection (i.e., with $S/N < 3$), we determine a lower limit on the EW following (61). Finally, we inspected each object by eye and removed four spurious sources that were lying in proximity to a bright star.

The final clean catalog consisted of 61 LAE candidates above a $\text{Ly}\alpha$ flux of limit of $5.4 \times 10^{-18} \text{ erg s}^{-1} \text{ cm}^{-2}$, over our $6' \times 7.8'$ imaging field-of-view, and the redshift range $z = 2.030 - 2.057$ spanned by the narrow-band filter. We estimated that our catalog is 50% (90%) complete above a flux limit of $F_{50} = 6.7 \times 10^{-18} \text{ erg s}^{-1} \text{ cm}^{-2}$ ($F_{90} = 7.4 \times 10^{-18} \text{ erg s}^{-1} \text{ cm}^{-2}$). This catalog of LAEs is presented in Table S4. In the following clustering analysis, we consider only those sources with rest-frame $W_{\text{Ly}\alpha} > 20\text{\AA}$ and a luminosity $\log_{10} L_{\text{Ly}\alpha} > 42.1$ which at $z = 2.04$ corresponds to a flux limit of $4.0 \times 10^{-17} \text{ erg s}^{-1} \text{ cm}^{-2}$. Given that this flux level is a factor

of five higher than the 90% completeness flux limit of our catalog, we are certain that we are complete to such sources. The f/g quasar lies at a distance of $2.08'$ from the edge of our imaging field, and for simplicity, our clustering analysis considers only the 10 sources within this radius which corresponds to a comoving impact parameter of $2.2 h^{-1} \text{ cMpc}$. Of these, 3/10 are the spectroscopically confirmed AGN1-3. The sources included in our clustering analysis are denoted by an asterisk in Table S4.

4.2 Clustering Analysis of HzRGs and LABs

We now describe how we used a compilation of LAEs around HzRGs and LABs to estimate the giant nebulae-LAE cross correlation function. The vast majority of $z \sim 2 - 3$ protoclusters in the literature have been identified and studied via overdensities of LAEs over comparable fields of view $6' \times 7.8'$ as our LRIS observations. For the HzRGs, we used a catalog of LAE positions around HzRGs from the survey of (13). Specifically, we focus on six HzRGs from the Venemans et al. study in the redshift range $z = 2.06 - 3.13$, which are approximately co-eval with SDSSJ0841+3921 at $z = 2.0412$. In addition to the six HzRGs from Venemans et al. (13), we also include two LABs at $z \sim 2 - 3$ from the literature whose environments have been surveyed for LAEs. Nestor et al. (106) conducted a narrow band imaging survey of the well known SSA22 protocluster field at $z = 3.10$. Their Keck/LRIS observations were centered on LAB1, whereas LAB2, the other known LAB in this field, resides at the edge of their imaging field. For this reason we only consider the overdensity around LAB1. Prescott et al. (19) conducted an intermediate-band imaging survey for LAEs around an LAB at $z = 2.66$ (LABd05) discovered by Dey et al. (16), finding a significant overdensity, and argued that the LAB resides in a protocluster. The eight objects used in our clustering analysis are listed in Table S5.

Given that the Venemans et al. sample (13) is the largest compilation of LAEs around HzRGs, and that, to our knowledge, the two LABs we consider are the only ones whose environments have been characterized using LAEs to a depth comparable to our observations, this sample of eight HzRGs/LABs is the only dataset currently available for conducting our clustering analysis and we believe that they comprise a fairly representative sample. Venemans et al. applied standard HzRG selection criteria to define their sample, and they published results for all HzRGs, not just those that hosted dramatic overdensities. Although LAB1 and LABd05 are larger and brighter than more typical LABs, they are comparable in size and luminosity to the HzRGs and to SDSSJ0841+3921, making for a fair comparison. One cause for concern is that the distribution of LAEs around the LABs were published specifically because these two systems resided in overdensities, and thus there may be a publication bias against LABs residing in lower density environments. Given that LABs only comprise a fourth of our clustering sample, we do not believe that this significantly biases our results, but repeating our clustering analysis for a larger and more uniformly selected sample of LABs would clearly be desirable.

Note that the HzRG MRC 1138–2262 included in our analysis is the famous Spider Web Galaxy protocluster, which has been the subject of extensive multi-wavelength follow-up, and

is one of the most dramatic protocluster systems known. Venemans et al. (13) argued that all of the HzRGs in Table S5 reside in overdensities of LAEs, with the exception of MRC 2048–272 and TN J20093040, for which the abundance of LAEs was found to be consistent with the field value, albeit with large error bars. We nevertheless include these two sources in our clustering analysis for several reasons. Our objective for the clustering analysis is to shed light on the connection between active SMBHs, large-scale Ly α nebulae, and protocluster environments. Given that it has been argued that the HzRGs as a population trace extremely overdense protocluster environments, and given that MRC 2048272 and TN J20093040 are both powerful HzRGs with large Ly α nebulae, excluding them from the analysis would be arbitrary, and would bias our correlation function high. Furthermore, the background number density of LAEs used by Venemans et al. (13) is rather outdated, the overdensity estimates have large error bars for individual systems, and the luminosity limits that they adopted for the LAEs in each field considered were heterogeneous. These factors complicate the interpretation, particularly if the clustering of LAEs is luminosity dependent. Hence our goal is to conduct a homogeneous analysis of the clustering of LAEs around the HzRGs/LABs which are above a uniform Ly α luminosity $\log_{10} L_{\text{Ly}\alpha} > 42.1$, without cherry picking specific objects. We adopt this luminosity limit for two reasons. First, the NB imaging observations for all eight objects listed in Table S5 are complete for identifying LAEs above this luminosity, mitigating uncertainties due to incompleteness. Second, this limit corresponds to the faintest luminosity for which the background number density of LAEs is well characterized (32); working fainter would thus require a significant extrapolation of the luminosity function, which would add systematic uncertainties to our results. For all of the objects analyzed (see Table S5), the LAE catalogs available are complete above the Ly α equivalent width limit of $W_{\text{Ly}\alpha} > 20\text{\AA}$ (the same value used to define our LAE catalog around SDSSJ0841+3921), with the exception of the Prescott et al. observations of the LAB LABd05. These observations used an intermediate band filter, and thus adopt a rest-frame $W_{\text{Ly}\alpha} > 40\text{\AA}$. We consistently account for this difference below when we compute the background number density of LAEs.

Given the small size of this HzRG/LAB dataset, we use an unbinned maximum likelihood estimator to determine the parameters r_0 and γ , following the procedure outlined in (107, 108). Specifically, we assume that the cross-correlation function between the giant nebulae (HzRGs/LABs) and LAEs obeys a power law form $\xi(r) \equiv (r/r_0)^{-\gamma}$. We use this correlation function to calculate the expected number of LAEs within a comoving cylindrical volume with transverse separation from R to $R + dR$, and half-height ΔZ , which is set by the width of the given narrow band filter $\Delta Z \equiv \text{FWHM}/(2aH(z))$, where $\text{FWHM} = c\Delta\lambda/\lambda$ is the full width half maximum of the filter in velocity units, $a = 1/(1+z)$ is the scale factor, $H(z)$ is the Hubble expansion rate, and division by $aH(z)$ converts velocities to comoving units. We imagine dividing the transverse separation R into a set of infinitesimal bins of width dR , such that each bin can contain only one or zero LAEs. Under the assumption that the clustering of

LAEs around the giant nebulae is a Poisson process, we can write the likelihood function as

$$\mathcal{L} = \left[\prod_i^{N_{\text{LAE}}} e^{-\mu_i} \mu_i \right] \left[\prod_{j \neq i} e^{-\mu_j} \right], \quad (6)$$

where $\mu = 4\pi R \Delta Z n_{\text{LAE}} [1 + h(R)] dR$ is the probability of finding a pair in the interval dR , the index i runs over the dR bins containing the N_{LAE} HzRG/LAB-LAE pairs in the sample, and the index j runs over all the bins for which there are no pairs. Here $n_{\text{LAE}}(> L_{\text{Ly}\alpha})$ is the number density of LAEs brighter than the survey limit $L_{\text{Ly}\alpha}$, and $h(R)$ is the cross-correlation function averaged over the filter width

$$h(R) = \frac{1}{2\Delta Z} \int_{-\Delta Z}^{\Delta Z} \xi(\sqrt{R^2 + Z^2}) dZ \quad (7)$$

Taking the natural logarithm of the likelihood, we have

$$\ln \mathcal{L} = \sum_i^{N_{\text{LAE}}} \ln [1 + h(R_i)] - 2n_{\text{LAE}} \Delta Z \int_{R_{\min}}^{R_{\max}} 2\pi R h(R) dR, \quad (8)$$

where we have dropped all additive terms which are independent of our model parameters (r_0, γ) , and $[R_{\min}, R_{\max}]$ is the range of comoving scales over which we search for HzRG/LAB-LAE pairs. In the following clustering analysis, we adopt $R_{\min} = 50 h^{-1} \text{ckpc}$ to minimize confusion with LAEs embedded in the respective nebulae, and $R_{\max} = 2.5 h^{-1} \text{cMpc}$, which is well matched to the maximum impact parameter probed $R = 2.2 h^{-1} \text{cMpc}$ around the f/g quasar. Given that the HzRGs and LABs in Table S5 all have different filter widths, as well as different $W_{\text{Ly}\alpha}$ limits and redshifts (which changes the background density n_{LAE}), the likelihood in eqn. (8) is specific to a single source. However, the full likelihood of the entire dataset given the model parameters, can be determined by simply summing log-likelihoods (multiplying the likelihoods) over all of the HzRGs/LABs, each of which has the form of eqn. (8),

Our clustering analysis relies on a determination of the field LAE luminosity function n_{LAE} . We use the Ciardullo et al. (32) Schechter function fits to the luminosity function from their own LAE survey at $z = 3.1$, and the Ciardullo et al. fits to the LAE survey data of (109) at $z = 2.1$. Both of these surveys are highly complete down to our limiting luminosity of $\log_{10} L_{\text{Ly}\alpha} > 42.1$ for LAEs with equivalent width $W_{\text{Ly}\alpha} > 20 \text{\AA}$. Ciardullo et al. also estimated the rest-frame equivalent width distribution, and found that LAEs follow an exponential distribution with rest-frame scale lengths of $W_0 = 50 \text{\AA}$ and $W_0 = 64 \text{\AA}$, at $z = 2.1$ and $z = 3.1$ respectively. Hence, for LABd05 which employed an $W_{\text{limit}} > 40 \text{\AA}$, we take the luminosity function of LAEs to be $n_{\text{LAE}}(> W_{\text{limit}}, > L_{\text{Ly}\alpha}) = \exp[-(W_{\text{limit}} - 20 \text{\AA})/W_0] n_{\text{LAE}}(> 20 \text{\AA}, > L_{\text{Ly}\alpha})$, where $n_{\text{LAE}}(> 20 \text{\AA}, > L_{\text{Ly}\alpha})$ are the Ciardullo et al. Schechter-function fits. To determine the luminosity function at intermediate redshifts between $z = 2.1$ and $z = 3.1$, we linearly interpolate.

In Fig. S4 we show confidence regions in the $r_0 - \gamma$ plane for the likelihood in eqn. (8). The maximum likelihood value is $r_0 = 29.3 h^{-1} \text{cMpc}$ and $\gamma = 1.5$, however a strong degeneracy exists between r_0 and γ , such that neither is individually well-determined. The low signal-to-noise ratio of the clustering measurement is partly to blame for this degeneracy, however it is also a consequence of the functional form adopted for the correlation function $\xi(r) \equiv (r/r_0)^{-\gamma}$, for which the amplitude and slope of the correlation function are not independent parameters.

Note that errors on the parameters r_0 and γ given by our maximum likelihood estimator in eqn. (8) and illustrated in Fig. S4 underestimate the true errors. This is because our likelihood explicitly assumes that the positions of the LAEs are completely independent draws from a Poisson process. This approach ignores correlations between the LAE positions (which are generically present for hierarchical clustering) and fluctuations due to cosmic variance. We opted for this unbinned estimator, because the traditional method of computing the correlation function in impact parameter bins, and fitting a power-law will, for such small samples, yield results which depend sensitively on the choice of binning, unless the covariance of the bins is included in the fit. The correct approach would be to fit the binned correlation function using the correct covariance matrix, whose off-diagonal elements would reflect the correlations between LAEs, and whose amplitude would include fluctuations due to sample variance. Given our limited sample size of eight HzRGs/LABs, the total number of LAEs in our clustering analysis is only 75, and there is no hope of computing the covariance from the data itself. In principle one could adopt a model for the covariance based on N -body simulations, but this would require a full model for how LAEs populate dark matter halos, and would be sensitive to the assumed masses of the protocluster halos. Such a detailed analysis is beyond the scope of the present work. As a compromise, we use the unbinned maximum likelihood estimator in eqn. (8) to determine our best fit model parameters, and we obtain estimates of the errors on parameters via a bootstrap technique. Specifically, we generate 1000 realizations of mock datasets, where a random sampling of the eight HzRGs/LABs in Table S5 are selected with replacement. Given that we are measuring a cross-correlation of LAEs around eight distinct objects, only the LAE positions arising from the same source are correlated, whereas the others are completely independent because of the large respective distances between the HzRGs/LABs. As such, for each of these 1000 realizations, we also bootstrap resample the positions of the LAEs around each object (with replacement), which encapsulates fluctuations due to correlations in the LAE positions and Poisson counting fluctuations. For each bootstrap realization of our dataset, we compute the parameters r_0 and γ via our maximum likelihood procedure, and determine errors on these parameters from the resulting distributions.

Based on this procedure, we define the 1σ confidence region from the 16th and 84th percentiles of the bootstrapped parameter distributions. We find a range $0.36 < \gamma < 1.98$ for γ , and $15.8 h^{-1} \text{cMpc} < r_0 < 9404 h^{-1} \text{cMpc}$. The correlation length r_0 is poorly constrained, because for flat correlation function slopes $\gamma < 1$, the clustering projected along the line-of-sight is very insensitive to r_0 , which again simply reflects the fact that the amplitude and slope of the correlation function are not independent parameters. This is the same behavior seen in the contours in Fig. S4. Fixing the slope γ to its maximum likelihood value of $\gamma = 1.5$, we

determine a 1σ confidence region for the cross-correlation length of $r_0 = 29.3 \pm 4.9 h^{-1} \text{ cMpc}$.

Although we do not fit the binned correlation function to determine model parameters, it is instructive to compute a binned correlation function to visualize the data, our model fits, and the errors on these fits. As such, we define a dimensionless correlation function as

$$\chi(R_i, R_{i+1}) \equiv \frac{\sum_j^{N_{\text{proto}}} \langle PG \rangle_{ij}}{\sum_{ij}^{N_{\text{proto}}} \langle PR \rangle_{ij}} - 1, \quad (9)$$

where $\langle PG \rangle_{ij}$ is the number of real HzRG/LAB-LAE pairs in the impact parameter bin $[R_i, R_{i+1}]$ around the j th object. The quantity $\langle PR \rangle_{ij} = n_{\text{LAE}}(z_j, > W_{\text{limit},j}) V_{ij}$ is the expected random number of pairs, which is simply the product of the background number density of LAEs, n_{LAE} , and the cylindrical volume, V_{ij} , defined by the bin $[R_i, R_{i+1}]$ and the half-height ΔZ_j of the NB filter used to survey the j th object. We compute errors on the binned correlation function via an analogous bootstrap method, whereby $\chi(R_i, R_{i+1})$ is recomputed from 1000 bootstrap resamplings of the sample of eight HzRGs/LABs while simultaneously bootstrap resampling the LAE separations from each object.

In Fig. S5, we show the binned correlation function calculated via this procedure, with 1σ error bars, determined by taking the 16th and 84th percentiles of the distribution of $\chi(R_i, R_{i+1})$ resulting from the bootstrap samples. For any value of the model parameters r_0 and γ , we can compute the predicted value of $\chi(R_i, R_{i+1})$ by evaluating the integrals

$$\langle PG \rangle_{ij} = n_{\text{LAE}}(z_j, > W_{\text{limit},j}) V_{ij} \int_{-\Delta Z_j}^{\Delta Z_j} \int_{R_i}^{R_{i+1}} [1 + \xi(\sqrt{R^2 + Z^2})] 2\pi R dR dZ, \quad (10)$$

and then evaluating the sum in eqn. (9). The uncertainty on the predicted clustering level, arising from the uncertainty on our model parameters, can thus be determined by evaluating the 16th to 84th percentile confidence region of the predicted $\chi(R_i, R_{i+1})$, using the distribution of r_0 and γ from the bootstrap resampling of our model fits. The resulting 1σ uncertainty on the predicted correlation function is shown as the gray shaded region in Fig. S5, with the maximum likelihood value $r_0 = 29.3 h^{-1} \text{ cMpc}$ and $\gamma = 1.5$ shown by the red curve. We see that our maximum likelihood model fit and bootstrap errors are consistent with the binned correlation function estimates and their respective errors.

Given the results of the clustering analysis described in this sub-section, we generate Fig. 2 of the main text as follows. Using our catalog of LAEs around the f/g quasar with $\log_{10} L_{\text{Ly}\alpha} > 42.1$ (Table S4), and the LAE luminosity function prediction for the background number density n_{LAE} , we can compute the cumulative overdensity profile $\delta(< R) \equiv 1 + \xi(R_{\text{min}}, R) = \langle PG \rangle / \langle PR \rangle$. The overdensity profile predicted by our maximum likelihood determination of r_0 and γ for the giant nebulae-LAE correlation function are determined by evaluating eqn. (10). This is shown as the red curve in Fig. 2. Similarly we can determine the 1σ error on the predicted $\delta(< R)$ by evaluating it for all of our bootstrap samples of r_0 and γ and taking the 16th-84th percentile region of the resulting $\delta(< R)$ distribution. This region is shown as the shaded grey area in Fig. 2. For comparison we show the expected overdensity (projected over our NB filter)

of Lyman break galaxies (LBGs) around radio-quiet quasars, based on the recent measurements of quasar-LBG clustering at $z \simeq 2.7$ by Trainor et al. (10), who found a cross-correlation length of $r_0 = 7.3 \pm 1.3 h^{-1} \text{ cMpc}$, assuming a fixed slope of $\gamma = 1.5$, similar to the best-fit slope deduced for our giant nebulae-LAE correlation. The blue dotted lines indicate the 1σ error quoted by Trainor et al. (10) on the cross-correlation length with the slope held fixed. Comparing to the Trainor et al. (10) measurements may seem questionable, given that: a) this is the cross-correlation with LBGs, whereas the clustering analysis in Fig. 2 is concerned with LAEs; b) the quasars studied by Trainor et al. were hyper-luminous. However, both of these differences are likely to produce small effects on the cross-correlation strength because a) the clustering of LAEs and LBGs are comparable at $z \sim 2.7$, and, assuming hierarchical clustering, the cross-correlation strength is only sensitive to the square-root of any differences in clustering strength; and b) the Trainor et al. (10) results are consistent, within the errors, with the quasar-LBG cross-correlation results of (110), who studied much fainter quasars. Indeed, both (110) and Trainor et al. (10) argue that the clustering of LBGs around quasars is independent of luminosity, assuaging concerns about comparing to hyper-luminous quasar clustering.

5 Near-IR Observations: The Systemic Redshift of the f/g Quasar

Quasar redshifts determined from the rest-frame ultraviolet emission lines (redshifted into the optical at $z \sim 2$) can differ by up to one thousand kilometers per second from the systemic frame, because of the complex motions of material in the broad line regions of quasars (94, 111). To achieve higher precision, one may analyze spectra of the narrow [O III] emission lines emerging from the narrow-line region, but at $z \sim 2$, this requires near-IR spectroscopy. On UT 2007 April 24, we obtained a near-IR spectrum of the f/g quasar (and also the b/g quasar) with the Near InfraRed Imager and Spectrometer (NIRI) on the Gemini North telescope. These data were reduced and calibrated with the LowRedux package, which performs wavelength calibration using the atmospheric sky lines recorded in each spectrum. With the chosen configuration, the spectra span $1.40 - 1.94 \mu\text{m}$ in the H-band.

Fig. S6 presents the NIRI spectra, fluxed with telluric standard stars taken that night. Each quasar shows the detection of strong [O III] emission and modest $H\beta$ emission. The [O III] $\lambda 5007$ lines were centroided using a flux-weighted line-centering algorithm with pixel values weighted by a Gaussian kernel, and this algorithm was iterated until the line center converged to within a specified tolerance (see (25) for more details). A small offset of 27 km s^{-1} was also added to the redshifts determined in this manner to account for average blueshift of the [O III] $\lambda 5007$ from systemic (111). We measured wavelength centroids of $\lambda_{\text{obs}} = 1.5231 \pm 0.0001 \mu\text{m}$ and $1.6095 \pm 0.00006 \mu\text{m}$ for the f/g and b/g quasars, respectively. This gives systemic redshifts $z_{\text{fg}} = 2.0412$ for the f/g quasar and 2.2138 for the b/g quasar. We estimate an uncertainty in this redshift of 50 km s^{-1} based on error in our wavelength calibration, line centering, and the estimated uncertainty when one uses [O III] to assess the systemic redshift of a quasar (111).

6 Kinematics

In the Main text, we described the complex kinematic motions of the quadruple AGN system and nebula as measured with slit spectroscopy (optical and near-IR; Figs. 3,S6) and absorption-line spectroscopy of a b/g quasar (Fig. 4). The AGN exhibit line-of-sight velocity differences of at least $\delta v = 1300 \text{ km s}^{-1}$, requiring extreme gravitational motions. Note that these large velocities cannot be explained by Hubble expansion. The miniscule probability of finding a quadruple quasar system in the absence of clustering $P \sim 10^{-13}$ (see Supp. 3), and the physical association between the AGN and giant nebula, demand that the four AGN reside in a real collapsed structure, and thus the relative motions of the AGN must result from gravitational motions in a collapsed structure.

The velocities of the nebular $\text{Ly}\alpha$ emission are also extreme, exhibiting line-of-sight velocities relative to the systemic redshift of f/g quasar ranging from $\delta v = -800$ to $+2500 \text{ km s}^{-1}$. These also trace the gravitational potential of the protocluster but may be influenced by other physical processes (e.g. kinematic or radiative feedback from the AGN). Finally, the absorption line kinematics of cool metal-enriched gas in the protocluster halo, measured from the b/g quasar spectrum, show strong absorption at $\approx +650 \text{ km s}^{-1}$ with a significant tail to velocities as large as $\simeq 1000 \text{ km s}^{-1}$.

We further emphasize two aspects here. First, although the nebular emission exhibits large, relative velocity offsets, the internal motions are relatively quiescent and generally unresolved at the Keck/LRIS spectral resolution ($\text{FWHM} \approx 160 \text{ km s}^{-1}$). There is no evidence for the “double-peaked” emission characteristic of resonantly trapped $\text{Ly}\alpha$. This implies that the gas within the nebula has modest opacity to $\text{Ly}\alpha$ photons and that the observed radiation is not predominantly scattered photons. These data also indicate that the gas motions are not strictly random, but are rather organized into coherent flows, i.e. the velocity offsets observed greatly exceed the measured velocity dispersions. Similar coherent motions have been previously observed in giant $\text{Ly}\alpha$ nebulae in HzRGs (112–115) and LABs (116).

Second, consider the gas kinematics along the single Slit 2 (Figs. 3 and S1). This slit covers the nebula from near the f/g quasar, where one observes a negligible velocity offset ($\delta v \approx 0 \text{ km s}^{-1}$), to the b/g quasar at $\approx 200 \text{ kpc}$ separation. As one travels along the slit, the velocity offset increases to $\simeq +500 \text{ km s}^{-1}$ as one approaches the b/g quasar, where the absorption-line spectrum shows a velocity offset of $\delta v \approx +650 \text{ km s}^{-1}$ (Fig. 4). Altogether, the gas along Slit 2 exhibits a velocity gradient of at least 500 km s^{-1} across 200 kpc (projected). These data establish the presence of large-scale, high-velocity flows of cool gas within this protocluster halo.

7 Estimates for the Abundance of Giant Ly α Nebulae Around Quasars

The protocluster SDSSJ0841+3921 was discovered because of its large-scale Ly α emission properties, and was selected from a well-defined survey for extended Ly α emission around 29 quasars (22). We can use the statistics of this survey to estimate the prevalence of giant Ly α nebulae around quasars. Insofar as there appears to be a physical connection between giant Ly α nebulae and protoclusters, this also provides insight into the prevalence of protoclusters around quasars. We also present an estimate for the frequency of occurrence of giant Ly α nebulae from an independent narrow-band imaging survey of quasars conducted by our group, and also discuss the results of similar narrow-band imaging surveys performed by others. Although much past work has been dedicated to characterizing Ly α nebulae around radio-loud quasar samples (117), it is only recently that sensitive observations have been undertaken to characterize the abundance of nebulae around predominantly radio-quiet quasars.

Our slit-spectroscopic observations allow us to estimate the effective covering factor of extended Ly α emission around the typical quasars ($L_{\text{bol}} \sim 10^{46} \text{ erg s}^{-1}$) we surveyed. Following the discussion in § 4.3 of (22; see Fig. 4 of that paper), large ~ 70 kpc scale nebulae can be detected down to $2 \times \text{SB}_{1\sigma}$, where $\text{SB}_{1\sigma}$ are the 1σ surface brightness limits quoted in Table 1 of (22). In that sample a nebula of comparable brightness to SDSSJ 0841+3921 $\text{SB}_{\text{Ly}\alpha} \simeq 10^{-17} \text{ erg s}^{-1} \text{ cm}^{-2} \text{ arcsec}^{-2}$ could have been detected at $> 2\sigma$ significance in 23/29 cases (see Table 1 of (22)). Based on this, we can crudely determine the covering factor of such filamentary emission as being the ratio of the area of the filament covered by our original slit observation of SDSSJ 0841+3921 (Slit2 in Figs. 3 and S1), to the total area surveyed at sensitivity sufficient to detect a $\text{SB}_{\text{Ly}\alpha} > 10^{-17} \text{ erg s}^{-1} \text{ cm}^{-2} \text{ arcsec}^{-2}$ nebula.

We consider an annular region around a $z = 2$ quasar with an inner radius of $R_{\perp, \text{min}} = 50 \text{ kpc}$ ($5.8''$) and outer radius of $R_{\perp, \text{max}} = 150 \text{ kpc}$ ($17.3''$). The inner radius is chosen to exclude the small-scale fuzz at $R_{\perp} < 50 \text{ kpc}$, which is detected in a large fraction of quasars (22), from the larger scale filamentary emission. The outer radius corresponds to the maximum extent of the (high significance) emission detected in our discovery spectrum of SDSSJ 0841+3921 (see Slit2 in Fig. 3 panel c, and the middle column of Fig. S1), and is about the virial radius of the dark matter halos $M_{\text{vir}} = 10^{12.5} M_{\odot}$ at $z = 2$ which host quasars (11). We also observe a drop-off in the covering factor of optically thick absorbers at $R_{\perp} \simeq 200 \text{ kpc}$, comparable to this $R_{\perp, \text{max}}$ (27). We assume the filamentary emission in the discovery spectrum extends from $+50 \text{ kpc}$ to $+150 \text{ kpc}$ at positive slit position, and -50 to -80 kpc at negative slit positions, corresponding to an area of 15 sq. arcsec given our $1''$ slit (1130 kpc^2). The total area is equal to the $N_{\text{QSO}} = 23$ quasars observed to sufficient depth, times the 23 sq. arcsec area (1740 kpc^2) for which our slit intersects the annular region, implying a total area of 530 sq. arcsec (39922 kpc^2) surveyed. For reference, the total annular area around a *single* quasar is 834 sq. arcsec (62832 kpc^2), so the effective area of our survey is 64% of the area around a single quasar. Hence we deduce a covering factor of filamentary emission of $f_{\text{C, fl}} = 0.028$.

Thus taken in aggregate, we find that only $\simeq 3\%$ of the area between $R_{\perp} = 50 - 150 \text{ kpc}$

around quasars is covered by Ly α emission with $SB_{Ly\alpha} > 10^{-17} \text{ erg s}^{-1} \text{ cm}^{-2} \text{ arcsec}^{-2}$, which can be compared to the much larger covering factor of 31% above this level, measured for emission over the same area from our NB image of SDSSJ0841+3921 (see Fig. 1a). The aggregate and individual covering factors can be commensurated if the majority of quasars do not exhibit large-scale Ly α nebulae above $SB_{Ly\alpha} > 10^{-17} \text{ erg s}^{-1} \text{ cm}^{-2} \text{ arcsec}^{-2}$, but a small fraction $\simeq 10\%$ have bright nebulae covering a large area, as in SDSSJ0841+3921, and the product of this $\sim 10\%$ frequency and $\sim 31\%$ covering factor set the aggregate $\sim 3\%$ effective covering factor for the entire population. This argument is consistent with our intuition that, given the random orientation of the slit, we could probably only have identified the asymmetric extended emission around SDSSJ0841+3921 for $\sim 50\%$ of the possible slit orientations, and given that 23 objects were surveyed to the required depth, this again suggests that $\sim 10\%$ of quasars exhibit giant nebulae.

An independent estimate for the frequency of giant Ly α nebulae around quasars can also be determined from a narrow band imaging survey conducted by our group. As part of a continuing program to search for fluorescent Ly α emission powered by luminous $z \sim 2$ quasars, to date we have obtained deep narrow band imaging of a sample of 26 objects. These survey observations are analogous to the narrow-band imaging of SDSSJ 0841+3921 discussed in Supp. 1.2, in that they use custom designed narrow-band filters, however the targets constitute an independent sample of quasars, which are not part of the QPQ survey of (22). These observations have been conducted on multiple telescopes, which we briefly summarize. For the present purposes we define a giant Ly α nebula to be extended emission on a scale $> 50 \text{ kpc}$ from the quasar with average $SB_{Ly\alpha} > 10^{-17} \text{ erg s}^{-1} \text{ cm}^{-2} \text{ arcsec}^{-2}$.

The quasar HE0109–3518 at $z = 2.41$ was observed with the Very Large Telescope/ -FOcal Reducer Spectrograph (VLT-FORS) using a custom designed narrow band filter ($\lambda_{\text{center}} = 4145\text{\AA}$, $\text{FWHM}_{\lambda} = 40\text{\AA}$) for a total exposure time of about 20 hours, achieving a sensitivity limit (1σ) of $SB_{Ly\alpha} = 8 \times 10^{-19} \text{ erg s}^{-1} \text{ cm}^{-2} \text{ arcsec}^{-2}$ (61). No extended Ly α nebula was discovered. We have imaged a total of eight quasars with the Keck LRIS imaging spectrometer, of which three were observed with a filter centered on Ly α redshifted to $z = 2.279$ ($\lambda_{\text{center}} = 3986\text{\AA}$, $\text{FWHM}_{\lambda} = 30\text{\AA}$), and five with one centered at $z = 2.190$ ($\lambda_{\text{center}} = 3878\text{\AA}$, $\text{FWHM}_{\lambda} = 30\text{\AA}$). The exposure times for the LRIS observations vary from 2 to 10 hours, resulting in sensitivity limits (1σ) ranging from $SB_{Ly\alpha} = 1.2 \times 10^{-18} \text{ erg s}^{-1} \text{ cm}^{-2} \text{ arcsec}^{-2}$ to 5×10^{-19} . These VLT/FORS and Keck/LRIS observations specifically targeted hyper-luminous quasars $V \lesssim 17$, with the goal of understanding fluorescent Ly α emission from dark-galaxies (61) and the quasar CGM (41), and led to the discovery of a giant Ly α nebula around the quasar UM287 at $z = 2.28$. Nebulae were not detected around any of the other quasars surveyed. Finally, using a custom filter centered on Ly α at $z = 2.253$ ($\lambda_{\text{center}} = 3955\text{\AA}$, $\text{FWHM}_{\lambda} = 30\text{\AA}$), we have observed a total of 17 quasars using the Gemini Multi Object Spectrograph (GMOS) on the telescope Gemini South. For the GMOS observations, a subset of 3 quasars were observed with longer integrations, typically 5 hours and achieving a depth of (1σ) $SB_{Ly\alpha} = 1.5 \times 10^{-18} \text{ erg s}^{-1} \text{ cm}^{-2} \text{ arcsec}^{-2}$; whereas the other 14 quasars were observed in a fast survey mode with typical exposure times of about 2 hours and depth $SB_{Ly\alpha} =$

$3 - 4 \times 10^{-18} \text{ erg s}^{-1} \text{ cm}^{-2} \text{ arcsec}^{-2}$. Although the instruments used and depths achieved are heterogeneous, all of the aforementioned observations reached sufficient depth to detect $\text{Ly}\alpha$ nebulae with $\text{SB}_{\text{Ly}\alpha} > 10^{-17} \text{ erg s}^{-1} \text{ cm}^{-2} \text{ arcsec}^{-2}$. Taking all of these observations together, we have observed a total of 26 quasars and detected a single giant $\text{Ly}\alpha$ nebula around UM287 (41), implying that $1/26 = 0.04$ of quasars host giant $\text{Ly}\alpha$ nebulae. Adopting the 1σ confidence interval appropriate for the Poisson distribution in the small number regime, we deduce that the frequency of occurrence of giant nebulae is in the range $3 - 9\%$.

Finally, an independent narrow band imaging survey of quasars at $z \sim 2.7$ is being carried out as part of the Keck Baryonic Structure Survey (KBSS), and the first results on the distribution of LAEs around quasars were recently published by Trainor et al. (118). Based on these narrow band imaging observations, (39) published the discovery and additional observations of a giant $\text{Ly}\alpha$ nebula around the quasar HS1549+19 with properties comparable to that around SDSSJ0841+3921. Trainor et al. quote a typical narrow-band imaging depth of $m_{\text{NB}}(3\sigma) \sim 26.7$ for point sources, resulting from 5-7hr integrations on Keck LRIS using filters with $\text{FWHM} \sim 80\text{\AA}$. This corresponds to a (1σ) $\text{SB}_{\text{Ly}\alpha} \simeq 1.5 \times 10^{-18} \text{ erg s}^{-1} \text{ cm}^{-2} \text{ arcsec}^{-2}$, which although shallower than our own Keck LRIS survey (owing to their wider filters), it is nevertheless sufficient to detect giant nebulae with $\text{SB}_{\text{Ly}\alpha} > 10^{-17} \text{ erg s}^{-1} \text{ cm}^{-2} \text{ arcsec}^{-2}$. There are 8 objects observed in the Trainor et al. sample, but it is unknown to us whether additional $\text{Ly}\alpha$ nebulae are present, besides that around HS1549+19. As such, one can place a lower limit on the frequency of giant $\text{Ly}\alpha$ nebulae to be $1/8 = 0.125$, or a 1σ Poisson confidence interval of $10 - 29\%$.

To summarize, three independent surveys indicate that the frequency of occurrence of giant $\text{Ly}\alpha$ nebulae around quasars is consistent with being $\simeq 10\%$, although there are still limitations due to relatively small samples, heterogeneity of the datasets, and the differences in the search techniques (narrow-band imaging versus spectroscopy).

8 The Environments of Other Quasars with Giant $\text{Ly}\alpha$ Nebulae and the Impact of $\text{Ly}\alpha$ Fluorescence

Although quasar clustering indicates that the majority of $z \sim 2$ quasars reside in moderate overdensities, we speculate that $\sim 10\%$ trace much more massive structures, and it is this subset which also exhibits giant $\text{Ly}\alpha$ nebulae. SDSSJ0841+3921 clearly supports this interpretation, but there are indeed other examples.

Of course, we also have NB imaging data for UM287, the quasar at $z = 2.27$ with a giant $\text{Ly}\alpha$ nebula recently discovered by our group (41). However, because UM287 is a hyper-luminous quasar, we cannot characterize its environment via the number counts of LAEs as we have for SDSSJ0841+3921. The reason for this is that distribution of LAEs on Mpc scales from hyper-luminous quasars is likely to be dramatically enhanced by $\text{Ly}\alpha$ fluorescence (61), and it is not straightforward to disentangle the fluorescence and clustering enhancements. For example, consider the hyper-luminous quasar HE0109–3518, the proto-typical case for $\text{Ly}\alpha$

fluorescence by dark-galaxies studied by (61). The number of LAEs within $R < 4 h^{-1} \text{ cMpc}$ of HE0109–3518 is ~ 8.5 times larger than the cosmic background number expected from the LAE luminosity function, whereas the quasar-LBG correlation function (a reasonable proxy for the quasar-LAE clustering) averaged over the volume probed by these narrow-band observations would only predict an enhancement of ~ 1.5 . One comes to similar conclusions about the number of LAEs discovered around the hyper-luminous quasars in the KBSS sample of (118). Progress on understanding the environment of UM287, and its relationship to the giant $\text{Ly}\alpha$ nebulae, will require a sample of galaxies selected via broad-band photometry (i.e. LBG selection), to avoid contamination from fluorescence. Nevertheless, while fluorescence precludes a simple interpretation of LAE clustering around UM287, we note that, intriguingly, follow-up observations also revealed a faint $V \simeq 22$ companion quasar, indicating an overdensity of AGN similar to SDSSJ0841+3921.

Note however that enhanced LAE clustering around SDSSJ0841+3921 due to $\text{Ly}\alpha$ fluorescence is expected to be negligible, because brightest quasar in the system, namely the f/g quasar with $V = 19.8$ is an order of magnitude fainter than the hyper-luminous quasars which exhibit this fluorescence effect. Radiative transfer simulations of $\text{Ly}\alpha$ fluorescence around quasars (61) supports this conclusion. Furthermore, the four AGN in SDSSJ0841+3921 clearly constitute a dramatic overdensity of AGN, and there is no way for $\text{Ly}\alpha$ fluorescence to enhance AGN clustering. Note that the other three AGN do not significantly enhance the ionizing luminosity and hence cannot boost the fluorescence signal. The fainter Type-1 AGN AGN2 and AGN3 have $V \simeq 23$ (see Table S2), and thus contribute negligibly to the total ionizing photon production compared to the f/g quasar. Although we do not detect the continuum from the accretion disk of the Type-2 AGN AGN1, it is detected in the WISE bands W1 and W2 (see Table S2). At $z \simeq 2$ these bands probe rest-frame $\sim 1 \mu\text{m}$, which are likely still dominated by emission from the reddest part of the accretion disk. The fact that AGN1 is > 1 magnitude fainter than the f/g quasar indicates that its UV ionizing continuum (although obscured from our perspective) is very unlikely to be brighter than that of the f/g quasar.

The KBSS quasar HS1549+19 at $z = 2.85$, which has been narrow band imaged by Trainor et al. (118), harbors a giant $\text{Ly}\alpha$ nebula (39) with SB and properties comparable to that around SDSSJ0841+3921. Extensive imaging and spectroscopy of HS1549+19 has demonstrated that it is clearly a dramatic protocluster, with a Mpc-scale overdensity of Lyman break galaxies (LBGs) a factor of ~ 3.5 times larger than that around typical quasars (10, 38). Although this quasar is hyper-luminous, $\text{Ly}\alpha$ fluorescence is not an issue because the protocluster overdensity is based on the clustering of broad-band selected LBGs, and not LAEs.

Finally, one may have concerns that the dramatic enhancements of LAEs around HzRGs and LABs, quantified by our clustering analysis in Supp. 4 and shown in Figs. 2 and S5, could be partly due to $\text{Ly}\alpha$ fluorescence. This is a valid concern, because there is compelling evidence that the HzRGs are obscured quasars (119), and their ionizing photons, although obscured from our perspective, surely shine in other directions, and are likely to power their giant $\text{Ly}\alpha$ nebulae. Similar considerations hold for LABs, although a direct association with obscured AGN has been more challenging to establish (18, 120–123). However, we think that it is unlikely that flu-

orescence plays a significant role in the strong clustering of LAEs around HzRGs and LABs for two reasons. First, there is no evidence that the unobscured counterparts of HzRGs and LABs (i.e. the Type-1 quasar shining in other directions) are as bright as the hyper-luminous $V \lesssim 17$ quasars, and hence sufficient to power LAE fluorescence on Mpc scales. Furthermore, even if the HzRGs and LABs were shining brightly in unobscured directions, the LAE enhancement is expected to be significantly smaller than for unobscured quasars, because given the cylindrical volume probed by NB imaging observations, the illuminated volume will be much larger for an unobscured quasar pointing toward the observer and hence along the major axis of the cylindrical survey volume, than for an obscured quasar which illuminates a volume randomly oriented relative to our line-of-sight direction (61).

Thus, although based on only a handful of objects, existing observations support a picture where $\sim 10\%$ of radio-quiet quasars are surrounded by giant $\text{Ly}\alpha$ nebulae, which acts as a signpost for the presence of a protocluster. A similar connection between AGN activity, giant $\text{Ly}\alpha$ nebulae, and protocluster overdensities has been suggested by past work on HzRGs and LABs. Our clustering analysis in Supp. 4 (see Figs. 2 and S5) demonstrates that these overdensities are indeed very large and well in excess of the environment of radio-quiet quasars. These protocluster overdensities are real, and are not the result of $\text{Ly}\alpha$ fluorescence.

9 Absorption Line Analysis

Given the experimental design of our QPQ survey, we are able to explore characteristics of the gas surrounding the quadruple AGN in unprecedented detail. Fig. 4 shows strong H I $\text{Ly}\alpha$ absorption coincident with the redshift of the protocluster. We measure a rest-frame equivalent width $W_\lambda = 3.75 \pm 0.05 \text{ \AA}$, offset by a velocity $\delta v = c\Delta\lambda/\lambda \approx +650 \text{ km s}^{-1}$ from the f/g quasar systemic redshift. The absence of very strong damping wings limits the H I column density to be $N_{\text{HI}} < 10^{19.7} \text{ cm}^{-2}$. We also present our favored model which has $N_{\text{HI}} = 10^{19.2 \pm 0.3} \text{ cm}^{-2}$, suggesting optically thick gas at the Lyman limit. It is possible, in the presence of significant line-blending, that the N_{HI} value could be much lower, but we consider this scenario very unlikely, since it would imply a gas metallicity exceeding the solar abundance (see below).

Fig. S7 presents spectra of the b/g quasar centered at the wavelengths of a series of strong, commonly observed UV resonance-line transitions (including the several transitions shown in Fig. 4 of the Main text) in the rest-frame of the f/g quasar (based on its near-IR systemic redshift). The gas exhibits especially strong low-ion absorption (O I 1302, C II 1334) and moderately strong intermediate ion absorption (N II 1083, Si III 1206). The latter absorption occurs within the $\text{Ly}\alpha$ forest and could be partially blended with coincident IGM absorption, but we believe such contamination is modest because the line-profiles track one another as well as the other low-ion transitions. Surprisingly, there is no statistically significant absorption at the high-ion transitions of Si^{+3} or C^{+3} . Even without performing a detailed photoionization analysis, we can already conclude that the gas is not highly ionized, which further suggests the gas is optically thick to ionizing radiation. One draws a similar conclusion from the relative strengths of

O I 1302 to Si II 1304, where the latter is observed to have larger equivalent width in systems that are highly ionized (e.g., (124, 125)), contrary to our measurements for this system.

For each of the absorption lines, we have estimated rest-frame equivalent widths with simple boxcar integration. Ionic column densities were estimated from the metal-line transitions assuming the linear curve-of-growth approximation and adopting lower limits to positive detections and upper limits for non-detections (Table S6). Because neutral oxygen O^0 undergoes charge-exchange reactions with atomic hydrogen, the ratio N_{O^0}/N_{HI} is very nearly equal to the number ratio O/H over a wide range of physical conditions and ionizing radiation fields (25). Therefore, we estimate a conservative lower limit to the oxygen metallicity $[O/H] > -1$. To estimate abundances of the other ions and to constrain physical conditions of the gas, we must evaluate the ionization state with photoionization models (see the next section).

Our previous studies have shown that cool gas with strong metal-line absorption from lower ionization states is common in the environment surrounding $z \sim 2$ quasars (26, 28). In Fig. S8 we show the distribution of equivalent widths for H I $Ly\alpha$ and C II 1334 from the set of QPQ pairs with separations less than 200 kpc. The absorption strength for SDSSJ0841+3921 lies toward the upper end of the distribution but is not extreme.

In Table S6 we include estimates for the abundances of the observed elements assuming ionization corrections from the photoionization model discussed below and $N_{HI} = 10^{19.2} \text{ cm}^{-2}$. The observations require $> 1/10$ solar metallicity and several measurements suggest solar (or even super-solar) enrichment.

10 Joint Constraints on Protocluster Gas in Absorption and Emission

Our preferred mechanism for powering the giant $Ly\alpha$ nebula in SDSSJ0841+3921 is fluorescent emission from gas in the CGM of the protocluster powered by the radiation from the f/g quasar, with the gas residing in a population of cool dense clouds which are optically thin ($N_{HI} < 10^{17.5}$) to ionizing radiation. Because our absorption line observations of the b/g quasar provide constraints on the gas properties in the protocluster, we adopt a novel approach of modeling the emission and absorption properties of this gas simultaneously, using the Cloudy photoionization code (126). First, we describe our model for the distribution of the cool clouds, and introduce simple analytical models for the fluorescent emission to build intuition about the scaling with gas properties. Then, we consider a sequence of photoionization models of the gas intercepted by the b/g sightline, which is however undetected in emission. Our absorption line measurements and photoionization modeling imply that the total cloud column density must be $\log_{10} N_H = 20.4 \pm 0.4$. Under the reasonable assumption that the $Ly\alpha$ emitting gas in the nebula has the same N_H as that detected in absorption, we then show that reproducing the emission level requires very high gas volume densities $n_H \simeq 2.0 \text{ cm}^{-3}$.

10.1 Cool Cloud Model and Emission Estimates

We consider an idealized model whereby the gas in the protocluster halo resides in a population of cool $T \sim 10^4$ K spherical gas clouds, which have a single uniform hydrogen volume density n_{H} and hydrogen column density N_{H} . The clouds are uniformly distributed throughout a spherical halo of radius R , and their aggregate covering factor, defined to be an average over the sphere, is f_{C} . Four parameters $(R, n_{\text{H}}, N_{\text{H}}, f_{\text{C}})$ completely describe the distribution of the gas (see (22) for further details), for example the total cool gas mass can be written

$$M_{\text{c}} = 3.3 \times 10^{11} \left(\frac{R}{250 \text{ kpc}} \right)^2 \left(\frac{N_{\text{H}}}{10^{20.5} \text{ cm}^{-2}} \right) \left(\frac{f_{\text{C}}}{0.5} \right) M_{\odot} \quad (11)$$

We now consider fluorescent $\text{Ly}\alpha$ emission from this population of cool gas clouds powered by a bright central quasar. There are two regimes where simple expressions can be obtained for the resulting emission, namely when the gas clouds are either optically thin $N_{\text{HI}} < 10^{17.5} \text{ cm}^{-2}$ or optically thick $N_{\text{HI}} > 10^{17.5} \text{ cm}^{-2}$ to Lyman continuum photons. For the optically thin case, the gas clouds are highly ionized, and the average $\text{Ly}\alpha$ SB from the halo will be

$$\text{SB}_{\text{Ly}\alpha} = 1.2 \times 10^{-17} \left(\frac{1+z}{3.0} \right)^{-4} \left(\frac{f_{\text{C}}}{0.5} \right) \left(\frac{n_{\text{H}}}{1.0 \text{ cm}^{-3}} \right) \left(\frac{N_{\text{H}}}{10^{20.5} \text{ cm}^{-2}} \right) \text{ erg s}^{-1} \text{ cm}^{-2} \text{ arcsec}^{-2}. \quad (12)$$

Note that because the gas is already highly-ionized, the SB is independent of the luminosity of the central ionizing source provided that it is bright enough to maintain the gas as optically thin.

If the clouds are optically thick to ionizing radiation, they will no longer emit $\text{Ly}\alpha$ proportional to the volume that they occupy because of self-shielding effects. Instead, a thin highly ionized skin will develop around each cloud, and nearly all recombinations and resulting $\text{Ly}\alpha$ photons will originate in this skin. The cloud will then behave like a ‘mirror’, converting a fraction $\eta_{\text{thick}} = 0.66$ of the ionizing photons it intercepts into $\text{Ly}\alpha$ photons (127). In this regime, it can be shown (see (22)) that the fluorescent SB, averaged over the halos is

$$\begin{aligned} \text{SB}_{\text{Ly}\alpha} &= \frac{\eta_{\text{thick}} h \nu_{\text{Ly}\alpha}}{4\pi(1+z)^4} f_{\text{C}} \Phi(R/\sqrt{3}) \\ &= 8.8 \times 10^{-17} \left(\frac{1+z}{3.0} \right)^{-4} \left(\frac{f_{\text{C}}}{0.5} \right) \left(\frac{R}{100 \text{ kpc}} \right)^{-2} \\ &\times \left(\frac{L_{\nu_{\text{LL}}}}{10^{30.5} \text{ erg s}^{-1} \text{ Hz}^{-1}} \right) \text{ erg s}^{-1} \text{ cm}^{-2} \text{ arcsec}^{-2}, \end{aligned} \quad (13)$$

where $h\nu_{\text{Ly}\alpha}$ is the energy of a $\text{Ly}\alpha$ photon and Φ ($\text{phot s}^{-1} \text{ cm}^{-2}$) is the ionizing photon number flux

$$\Phi = \int_{\nu_{\text{LL}}}^{\infty} \frac{F_{\nu}}{h\nu} d\nu = \frac{1}{4\pi r^2} \int_{\nu_{\text{LL}}}^{\infty} \frac{L_{\nu}}{h\nu} d\nu. \quad (14)$$

To obtain the second equality in eqn (13), we assume that the quasar spectral energy distribution obeys the power-law form $L_{\nu} = L_{\nu_{\text{LL}}} (\nu/\nu_{\text{LL}})^{\alpha_{\text{UV}}}$, blueward of ν_{LL} and adopt a slope of

$\alpha_{\text{UV}} = -1.7$ consistent with the measurements of (128). The quasar ionizing luminosity is then parameterized by $L_{\nu_{\text{LL}}}$, the specific luminosity at the Lyman edge. As we describe in detail below, we estimate that f/g quasar has $\log_{10} L_{\nu_{\text{LL}}} = 30.5$, which is the value adopted in eqn. (13). In the optically thick regime, we see that the SB now depends on the luminosity of the quasar, as well as on the covering factor f_{C} , but is independent of the gas properties (i.e. n_{H} and N_{H}).

The smooth morphology of the emission in the $\text{Ly}\alpha$ nebula implies a covering factor of $f_{\text{C}} \gtrsim 0.5$. Even if the emitting clouds have angular sizes much smaller than the PSF of our NB imaging, the morphology of the nebular emission would appear much more clumpy for lower covering factors. We have explicitly verified this by generating simulated images of mock $\text{Ly}\alpha$ emission distributions with the required SB and a range of covering factors f_{C} , and then convolving them with our NB-imaging PSF (129). In what follows we will always assume a covering factor of $f_{\text{C}} = 0.5$ for both the gas we detect in emission, as well as that detected in absorption. This value is well motivated: a) for the emission it is based on the smooth morphology of the nebula; b) for the absorption it is approximately the covering factor of optically thick absorbers on $R \lesssim 200$ kpc scales in the quasar CGM (27).

The average SB of the giant $\text{Ly}\alpha$ nebula at $R \simeq 100$ kpc is $\text{SB}_{\text{Ly}\alpha} = 1.3 \times 10^{-17} \text{ erg s}^{-1} \text{ cm}^{-2} \text{ arcsec}^{-2}$, which we compute via the emission from the area within our 2σ SB contour which intersects the the annulus $R = [75, 125]$ kpc. This is several times lower than the expectation from eqn. (13) for the optically thick regime. Thus our simple analytical scaling relations already appear to favor a situation where the clouds are optically thin. We return to this comparison below using photoionization models.

10.2 Details of Cloudy Modeling

The expressions in eqns. (12) and (13) provide reasonable estimates for the fluorescent SB, but they neglect other sources of $\text{Ly}\alpha$ emission such as collisional excitation (i.e. cooling radiation), and pumped or ‘scattered’ $\text{Ly}\alpha$ photons arising from the diffuse continuum produced by the gas itself. Note that we do not attempt to model scattering of $\text{Ly}\alpha$ photons produced by central f/g quasar itself. Radiative transfer simulations of radiation from a hyper-luminous quasar through a simulated gas distribution (41), have shown that the contribution of scattered $\text{Ly}\alpha$ line photons from the quasar do not contribute significantly to the $\text{Ly}\alpha$ surface brightness of the nebula. Given that this calculation was for a hyper-luminous quasar a factor of ~ 10 times brighter than the f/g quasar, scattered line photons from the quasar are expected to contribute negligibly to the nebular emission., and they also do not treat the temperature dependence of the emission. To fully account for these effects, we construct photoionization models for a slab of gas being illuminated by a quasar using the Cloudy software package (126). Cloudy predicts the emergent spectrum from the gas, allowing us to compute its SB, which we then dilute by the covering factor $f_{\text{C}} = 0.5$.

We model the quasar spectral-energy distribution (SED) using a composite quasar spectrum which has been corrected for IGM absorption (128). This IGM corrected composite is important because it allows us to relate the g -band magnitude of the f/g quasar to the specific luminosity

at the Lyman limit $L_{\nu_{\text{LL}}}$. For energies greater than one Rydberg, we assume a power law form $L_{\nu} = L_{\nu_{\text{LL}}}(\nu/\nu_{\text{LL}})^{\alpha_{\text{UV}}}$ and adopt a slope of $\alpha_{\text{UV}} = -1.7$, consistent with the measurements of (128). We determine the normalization $L_{\nu_{\text{LL}}}$ by integrating the Lusso et al. (128) composite spectrum against the SDSS filter curve, and choosing the amplitude to give the correct g -band magnitude of the f/g quasar (see Table S2), which gives a value of $\log_{10} L_{\nu_{\text{LL}}} = 30.5$. We extend this UV power law to an energy of 30 Rydberg, at which point a slightly different power law is chosen $\alpha = -1.65$, such that we obtain the correct value for the specific luminosity at 2 keV $L_{\nu}(2 \text{ keV})$ implied by measurements of α_{OX} , defined to be $L_{\nu}(2 \text{ keV})/L_{\nu}(2500 \text{ \AA}) \equiv (\nu_{2 \text{ keV}}/\nu_{2500 \text{ \AA}})^{\alpha_{\text{OX}}}$. We adopt the value $\alpha_{\text{OX}} = -1.5$ measured by (130) for SDSS quasars of comparable luminosities. An X-ray slope of $\alpha_{\text{X}} = -1$, which is flat in νf_{ν} is adopted in the interval of 2-100 keV, and above 100 keV, we adopt a hard X-ray slope of $\alpha_{\text{HX}} = -2$. For the rest-frame optical to mid-IR part of the SED, we splice together the composite spectra of (128), (84), and (131). These assumptions about the SED are essentially the standard ones used in photoionization modeling of AGN (e.g. (132)). We also include the contribution from the radiation field of the ambient UV background radiation field using the spectrum of (133), but it is completely sub-dominant relative to the f/g quasar at the distances that we consider.

These Cloudy models require as an input the ionizing photon number flux $\Phi(r)$ (see eqn. (14)) at the surface of the cloud. Because this varies with radius as r^{-2} , in principle modeling the halo emission would require integrating over a distinct photoionization model at each radius. For simplicity, we restrict attention to just a few radii. For our model of the optically thick absorber, we set $r = 250 \text{ kpc}$, which we believe is the likely location of the absorbing gas for several reasons. First, the nebula itself has an end-to-end size of $\simeq 500 \text{ kpc}$ roughly centered on the f/g quasar, such that $r = 250 \text{ kpc}$ is a reasonable radius for the absorber given the measured impact parameter $R_{\perp} = 176 \text{ kpc}$ of the b/g quasar sightline. Second, given this impact parameter, the characteristic velocity separation of the absorbing gas from systematic $v_{\text{max}} = 600 \text{ km s}^{-1}$ implied by the metal-line absorption (see Fig. S7), we can compute the conditional probability distribution $P(< r | R_{\perp}, v_{\text{max}})$ that the distance between the quasar and the absorber is less than r , which is determined by the quasar-LLS correlation function which we have measured (24, 27). For the problem at hand, we find that $P(< r | R_{\perp}, v_{\text{max}}) = 0.43$ for $r = 250 \text{ kpc}$, again indicating that this is a reasonable distance (see a similar discussion in § 4.1 of (25)). According to eqn. (13), the SB arising from such optically thick gas scales with Φ , and hence will decrease as r^{-2} . For the gas producing the Ly α emission, we model three radii $r = [50, 100, 250] \text{ kpc}$. We will argue that the emitting gas in the nebula is optically thin, and in this regime the SB is independent of Φ (see eqn. (12)). Thus considering a few radii to describe the emission is a reasonable approximation provided the gas remains optically thin at the radii in question.

The Cloudy model of the cool cloud is completely specified by the value of Φ , the SED shape, the metallicity of the gas Z , the hydrogen volume density n_{H} , and a ‘stopping criterion’, which sets the total column density of the cloud. Because we assume the f/g quasar and UVB are the only sources of ionizing photons, Φ and the SED shapes are fixed. For the metallicity, we adopt a value of $\log(Z/Z_{\odot}) = -0.5$ consistent with our lower-limit ($\log(Z/Z_{\odot}) > -1$) on

the metallicity of the optically thick absorber detected in the b/g quasar sightline (see Supp. 9). We have confirmed that the results discussed below are insensitive to the assumed gas metallicity. We have also verified that our results are insensitive to the exact value of the UV slope $\alpha = -1.7$, within the 1σ error measured by Lusso et al. $\alpha = -1.7 \pm 0.6$. Our models thus constitute a one-dimensional sequence parameterized by the volume density of the clouds n_{H} . Photoionization models are known to be self-similar in the ionization parameter $U = \Phi/n_{\text{H}}c$, which is the ratio of the number density of ionizing photons to hydrogen atoms. Since Φ has been fixed, our sequence of models is thus also a sequence in U , spanning the relevant range of ionization conditions. Our stopping criterion depends on what is known about the gas that we are attempting to model, which we elaborate on next.

10.3 Photoionization Model of the Absorbing Gas

Here we compare photoionization models to the properties of the optically thick absorber in the spectrum of the b/g quasar, lying at an impact parameter of $R_{\perp} = 176$ kpc from the f/g quasar. We follow the standard approach (25) and focus our analysis on multiple ionization states of individual elements to avoid uncertainties related to intrinsic abundances. Specifically, our column density measurements in Table S6 yield the following limits on ionic ratios: $\text{C}^+/\text{C}^{3+} > 0.8$, $\text{Si}^+/\text{Si}^{3+} > 1.3$, and $\text{Si}^+/\text{Si}^{2+} < 0.7$. In addition, we measured the neutral column density to be $N_{\text{HI}} = 10^{19.2} \text{ cm}^{-2}$, which we use as the stopping criterion of the Cloudy model. In other words, Cloudy will continue to add slabs of material until this neutral column is reached, guaranteeing that we satisfy this constraint. Finally, we do not detect Ly α emission from the vicinity of the background sightline, allowing us to set an upper limit of $\text{SB}_{\text{Ly}\alpha} < 5.1 \times 10^{-18} \text{ erg s}^{-1} \text{ cm}^{-2} \text{ arcsec}^{-2}$ from the cool gas. This SB limit was computed via simulations whereby a fake circular source with radius of $3''$ was placed at the location of the b/g quasar. This exercise showed that only sources with $\text{SB}_{\text{Ly}\alpha} > 3 \times \text{SB}_{1\sigma}$ would be clearly detectable, where $\text{SB}_{1\sigma} = 1.7 \times 10^{-18} \text{ erg s}^{-1} \text{ cm}^{-2} \text{ arcsec}^{-2}$ is our 1σ SB limit for 1.0 sq. arcsec apertures. Note that the individual clouds intercepted by our sightline may have extremely small sizes $\sim 10 \text{ pc}$ making it impossible to angularly resolve emission from a single cloud. However, we have argued that these clouds have a large covering factor of $f_{\text{C}} = 0.5$ such that we would be able to detect their aggregate emission near the location of the b/g sightline (see Fig. 1 in (22) for more details).

Our sequence of photoionization models is compared to the observational constraints in Fig. S9. The three different ionic ratios considered paint a consistent picture for the ionization state, and we constrain the ionization parameter to be $\log_{10} U = -2.7 \pm 0.3$, where we conservatively include an error of 0.3 dex to account for both statistical and systematic uncertainties in the photoionization modeling. Accordingly, the neutral fraction is constrained to be $\log_{10} x_{\text{HI}} = -1.2 \pm 0.3$, and the total hydrogen column $\log_{10} N_{\text{H}} = 20.4 \pm 0.4$, where the error on N_{H} includes the quadrature sum of modeling uncertainty in the neutral fraction, and the uncertainty in our measurement of N_{HI} (see Supp. 9). Plugging this determination of the total hydrogen column density into eqn. (11) we obtain a total cool gas mass of $M_{\text{c}} = 2.4 \times 10^{11} M_{\odot}$

within a spherical halo $R = 250$ kpc, or the range $1.0 \times 10^{11} M_{\odot} < M_c < 6.5 \times 10^{11} M_{\odot}$ implied by the 1σ measurement and modeling error on N_{H} . Note that given the self-similarity of the photoionization models with ionization parameter U , these results are essentially independent of the value of Φ that we have assumed in our models, and hence the distance of the gas from the quasar. Lastly, we have calculated the ionization corrections to the ionic column densities measured for the absorbing gas and provide limits on the elemental abundances implied by each metal absorption line measurement in Table S6.

According to the photoionization models, if indeed the absorbing gas lies at a distance $r = 250$ kpc and is illuminated by the f/g quasar, the $\text{Ly}\alpha$ emission would be $\text{SB}_{\text{Ly}\alpha} \simeq 3 - 4 \times 10^{-18} \text{ erg s}^{-1} \text{ cm}^{-2} \text{ arcsec}^{-2}$, which lies just below our detection limit $\text{SB}_{\text{Ly}\alpha} = 5.1 \times 10^{-18} \text{ erg s}^{-1} \text{ cm}^{-2} \text{ arcsec}^{-2}$, and is hence consistent with our non-detection of extended emission near the b/g quasar sightline. Indeed, because the gas is optically thick, and essentially absorbs all ionizing photons that impinge on it, the $\text{SB}_{\text{Ly}\alpha}$ is nearly independent of the volume density, and as expected from eqn. (13), depends primarily on Φ and our assumed covering factor $f_C = 0.5$. The weak dependence on n_{H} arises because, at the lowest ionization parameters and hence highest neutral fractions, as much as $\sim 20\%$ of the $\text{Ly}\alpha$ is produced by collisional excitation (green curve labeled collisions in Fig. S9). This is because collisional excitation of neutral hydrogen requires a large neutral fraction, and it is also exponentially sensitive to temperature. The low $n_{\text{H}} \lesssim 10^{-2} \text{ cm}^3$ and high ionization parameter $\log_{10} U \gtrsim -1$ models are highly ionized $x_{\text{HI}} \lesssim 10^{-3}$, and have higher temperatures $T \gtrsim 17,000$ K, both of which tend to suppress collisional excitation. As a result of the very weak dependence of $\text{SB}_{\text{Ly}\alpha}$ on n_{H} in the optically thick regime, our non-detection of emission does not allow us to put interesting constraints on the volume density n_{H} for the absorbing gas.

Note that the fact that our photoionization model predicts $\text{Ly}\alpha$ emission from the absorbing gas just below our detection limit results from our assumed distance of $r = 250$ kpc, since for optically thick gas $\text{SB}_{\text{Ly}\alpha} \propto \phi \propto r^{-2}$ (see eqn. 13). Had we assumed a distance equal to the impact parameter $R_{\perp} = 176$ kpc the predicted emission would be a factor of two higher $\text{SB}_{\text{Ly}\alpha} \sim 10^{-17} \text{ erg s}^{-1} \text{ cm}^{-2} \text{ arcsec}^{-2}$, and hence detectable. As such it is informative to briefly discuss all possible scenarios that would result in a non-detection of $\text{Ly}\alpha$ from the absorbing gas. These are: 1) the gas is illuminated by the f/g quasar, but it lies at a distance $r \gtrsim 250$ kpc such that its fluorescent $\text{Ly}\alpha$ emission is below our detection threshold; 2) the gas is illuminated by the quasar and is at a distance comparable to the impact parameter, but the covering factor of optically thick gas is much lower than we have assumed $f_C = 0.5$; 3) the absorbing gas is not illuminated by the f/g quasar but is instead shadowed, perhaps because from its vantage point the quasar is extinguished by the same obscuring medium invoked in AGN unification models (67, 68).

Unfortunately, our current observations cannot distinguish between these three scenarios, however we favor scenario 1), that the gas lies at a distance $\simeq 250$ kpc from the quasar, as shown in Fig. S9. While it is possible that the covering factor of optically thick gas is indeed lower than the $f_C = 0.5$ that we have assumed, we consider this unlikely for two reasons. First, this would be in conflict with the statistical properties of optically thick absorption for the aggregate population of quasars (27). Although, SDSSJ0841+3921 is atypical given that it is

a protocluster and hosts a giant nebula, we already argued that the smooth morphology of the giant nebula also argues for a high covering factor $f_C \gtrsim 0.5$ of the emitting gas, to prevent the emission from appearing too clumpy. Under the reasonable assumption that the absorbing and emitting gas have the same origin, one expects their covering factors to be comparable.

At first glance, the possibility that the absorbing gas is shadowed from the quasar radiation seems quite plausible. Indeed, we have previously argued in the QPQ series that the anisotropic clustering of LLSs around quasars implies that the optically thick gas in the quasar CGM is often shadowed (22–24). However, we robustly determine the ionization parameter of the absorbing gas to be $\log_{10} U = -2.7 \pm 0.3$. If obscuration shadows the gas from the quasar, then the radiation field would be expected to be the UV background, which given our ionization parameter, would then imply a gas density $n_H \sim 10^{-3} \text{ cm}^{-3}$. In the next section, we will see that the detection of bright $\text{Ly}\alpha$ emission implies that the density of the emitting gas is three orders of magnitude higher $n_H \sim 1 \text{ cm}^{-3}$. As indicated in the middle panel of Fig. S9, if the gas is illuminated by the quasar at a distance $r = 250 \text{ kpc}$, then gas density implied by our ionization parameter is then $n_H \simeq 0.7 \text{ cm}^{-3}$, which is then consistent with the value deduced from modeling the emission. Thus again invoking the very reasonable assumption that the absorbing and emitting gas have the same origin, the fact that we infer a comparable n_H for the absorbing gas as required for the emitting gas, seems to favor a scenario where the absorbing gas is illuminated by the f/g quasar, but lies at a distance $r \gtrsim 250 \text{ kpc}$, such that the fluorescent $\text{Ly}\alpha$ is below our threshold. Future deeper $\text{Ly}\alpha$ observations could test this hypothesis if they can reach $\text{SB}_{\text{Ly}\alpha} \simeq 10^{-18} \text{ erg s}^{-1} \text{ cm}^{-2} \text{ arcsec}^{-2}$ levels, such that one could then detect emission from the absorbing gas out to a distance as far as $r \simeq 500 \text{ kpc}$.

10.4 Photoionization Model of the Emitting Gas

Here we consider photoionization models for the emitting gas under the assumption that it has a comparable column density N_H to the gas we detect in absorption. In modeling the emission we consider gas at $r = 100 \text{ kpc}$ which is the characteristic scale of the emission nebula. We assume that the total hydrogen column density does not vary strongly between these distances. This hypothesis is supported by a photoionization modeling study of a large sample of quasar CGM absorbers, which indicates that on average the total column density N_H varies weakly (if at all) with impact parameter on such scales. We run the same Cloudy photoionization models as described previously, but with the modification that the stopping criterion is now chosen to be that the total hydrogen column $N_H = 10^{20.4} \text{ cm}^{-2}$, deduced in the previous section.

In Fig. S10 we show the results of our sequence of photoionization models for the $\text{Ly}\alpha$ emitting gas. The black curve illustrates the dependence of $\text{SB}_{\text{Ly}\alpha}$ on volume density n_H for our fiducial choice of the radiation field intensity, where the gas lies at a distance of $r = 100 \text{ kpc}$. The upper x-axis indicates the corresponding ionization parameter U at this distance. The red and blue curves are for stronger and weaker radiation fields, corresponding to $r = 50 \text{ kpc}$ and $r = 250 \text{ kpc}$, respectively. For low values of n_H the gas remains optically thin $N_{\text{HI}} \lesssim 10^{17.5} \text{ cm}^{-2}$, and the $\text{SB}_{\text{Ly}\alpha}$ exhibits a nearly linear dependence on the volume density n_H and

is nearly independent of the ionizing radiation intensity, as predicted by eqn. (12). The gas becomes self-shielding and optically thick once $N_{\text{HI}} \gtrsim 10^{17.5} \text{ cm}^{-2}$, at which point the $\text{SB}_{\text{Ly}\alpha}$ plateaus at a single value depending only on Φ (since we have fixed the covering factor $f_{\text{C}} = 0.5$) and hence on distance r , as predicted by eqn. (13).

These models clearly indicate that, given the column density of cool material $N_{\text{H}} = 10^{20.4} \text{ cm}^{-2}$, the volume density must be $n_{\text{H}} \simeq 2.0 \text{ cm}^{-3}$, in order to reproduce the observed average emission level at 100 kpc of $\text{SB}_{\text{Ly}\alpha} = 1.3 \times 10^{-17} \text{ erg s}^{-1} \text{ cm}^{-2} \text{ arcsec}^{-2}$ (indicated by the horizontal dashed line in Fig. S10). Provided that the emitting gas is optically thin $N_{\text{HI}} \lesssim 10^{17.5}$, this conclusion is essentially independent of the radiation field and hence the assumed distance of the gas from the f/g quasar. In this regard, the relatively flat radial $\text{SB}_{\text{Ly}\alpha}$ profile observed for the giant nebula is readily explained. It naturally arises because order of magnitude variations in the radiation field, corresponding to gas at distances ranging from $r = 50 - 200 \text{ kpc}$, produce nearly the same level of $\text{Ly}\alpha$ emission, provided that N_{H} does not vary significantly across the nebula, as we have assumed.

A corollary of our absorption-line constraint on $N_{\text{H}} \simeq 10^{20.4} \text{ cm}^{-2}$ and our emission constraint on $n_{\text{H}} \simeq 2.0 \text{ cm}^{-3}$ is that the implied absorption path length through the cool clouds is $l_{\text{cloud}} \equiv N_{\text{H}}/n_{\text{H}} \sim 40 \text{ pc}$, implying that the emitting gas is distributed in extremely compact dense clouds.

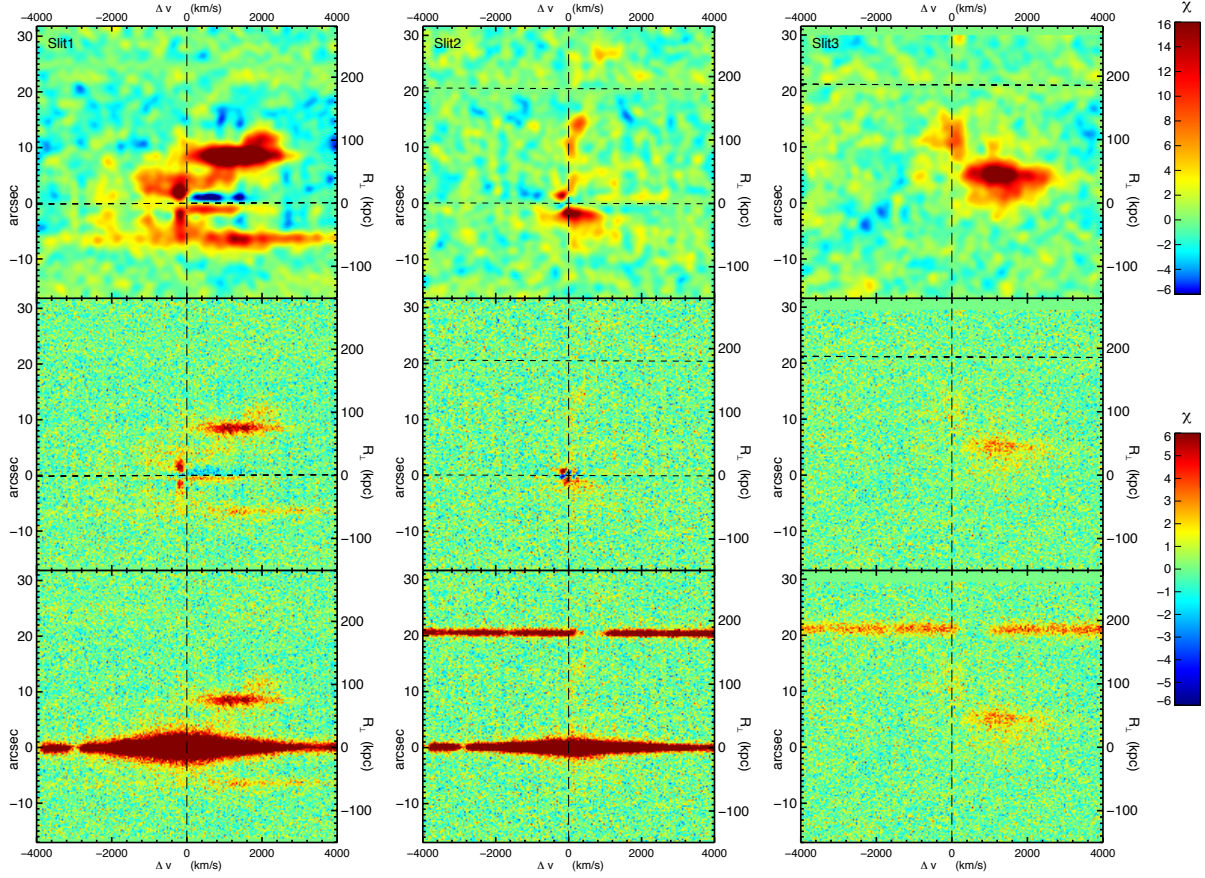


Fig. S1: Two dimensional spectrum plotted as a χ -map for the three slits in Fig. 3. The lower and middle rows of each image show χ_{sky} (sky-subtracted only) and $\chi_{\text{sky+PSF}}$ (sky and PSF subtracted), respectively as defined in § 1 (see (22) for additional details). The upper row shows the smoothed map χ_{smth} , (sky and PSF subtracted, then smoothed), which is helpful for identifying extended emission. A symmetric Gaussian kernel (same spatial and spectral widths in pixels) was adopted, with dispersion $\sigma_{\text{smth}} = 100 \text{ km s}^{-1}$ (FWHM = 235 km s^{-1}), and 1σ spatial smoothing of $0.65''$ (FWHM= $1.5''$). In the absence of extended emission, the distribution of pixel values in the the sky and PSF subtracted images should be Gaussian with unit variance. The lower and middle rows are displayed with a linear stretch ranging from -6σ to 6σ indicated by the color-bar at middle right. The upper row has a stretch from -6σ to 16σ is adopted, and a γ value chosen to decrease the range of color at the highest significance, as indicated by the color-bar at upper right. The horizontal dashed lines indicates the spectral traces for the f/g and b/g quasar, and the vertical dashed line indicates $\Delta v = 0$, corresponding to the systemic redshift of the f/g quasar. Note that the b/g quasar spectrum in Slit3 (right) has much lower S/N ratio than in Slit2 (center) because of much poorer seeing.

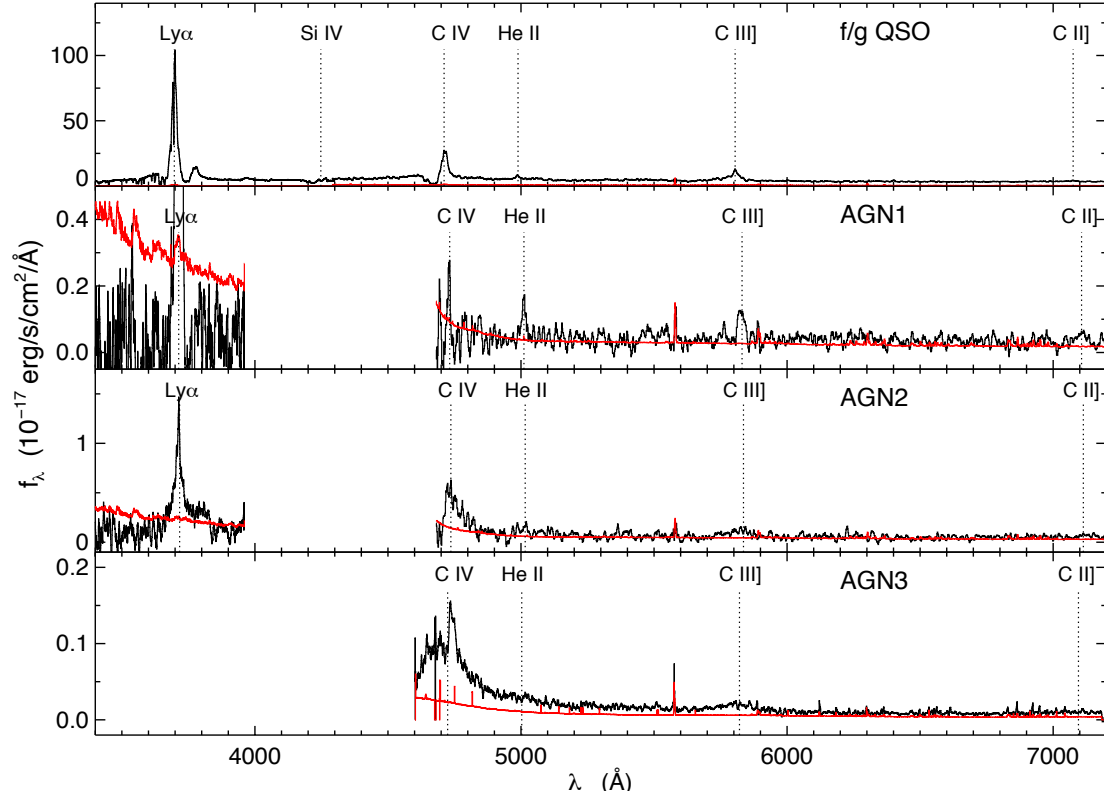


Fig. S2: Optical spectra of the four AGN at the same redshift. From top to bottom: f/g quasar, AGN1, AGN2, and AGN3. The gaps in the coverage of the spectra of AGN1 and AGN2 are due to the LRIS configuration chosen to cover both $\text{Ly}\alpha$, C IV, and He II. The spectrum of AGN3 does not cover the $\text{Ly}\alpha$ line due to the limited blue sensitivity of DEIMOS. Note the different scale on the y-axis to better show the different emission lines, which are marked with vertical dotted lines and labeled.

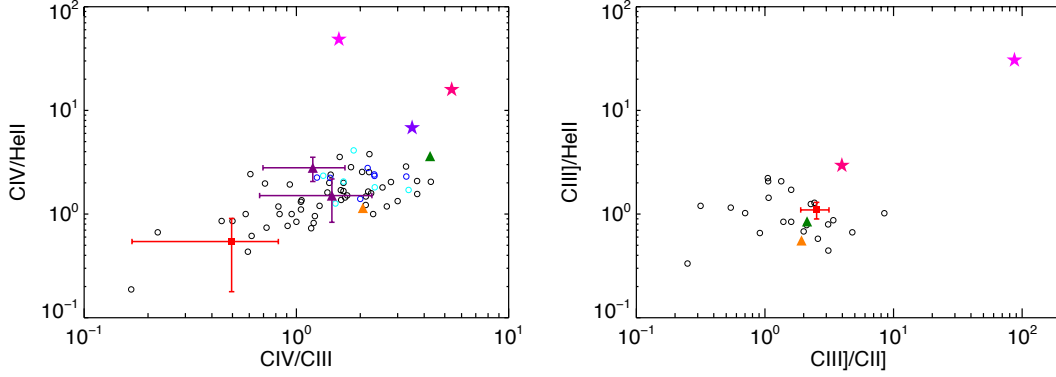


Fig. S3: Comparison of the Line-ratios of AGN1 to other Type-2 AGN. The line-ratios of AGN1 (red square) are compared to other Type-2 AGN compiled from the literature in the $C\text{ IV}/\text{He II}$ vs $C\text{ IV}/C\text{ III}]$ plane (left) as well as the $C\text{ III]}/\text{He II}$ vs $C\text{ III]}/C\text{ II}]$ plane (right). The circles are individual measurements of HzRGs (black) from the compilation of (80), and narrow-line X-ray sources (cyan) and Seyfert-2s (blue) from the compilation of (81). Triangles indicate measurements from the composite spectra of HzRGs (orange) from (70), the composite Type-2 AGN spectra (purple) from (82), who split their population into two samples above and below $\text{Ly}\alpha$ EW of 63\AA , and a composite spectrum of mid-IR selected Type-2 AGN (green) from (83). The stars represent measurements from composite spectra of Type-1 quasars, based on the analysis of (magenta) (84), (red-magenta) (85), and (blue-magenta) (86). The line-ratios for AGN1 lie in the locus of points spanned by other Type-2 objects in the literature.

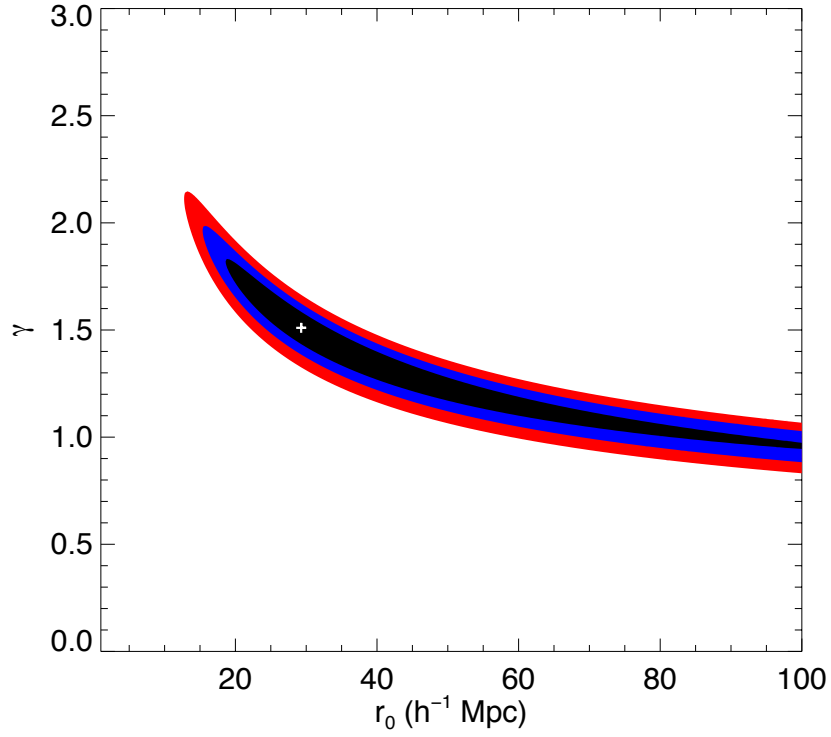


Fig. S4: Confidence regions on correlation function parameters from maximum likelihood clustering analysis. The 1, 2, and 3σ confidence regions are illustrated by the black, blue, and red contours, respectively. The maximum likelihood value is $r_0 = 29.3 h^{-1} \text{ Mpc}$ and $\gamma = 1.5$, which is indicated by the white cross. Due to the low signal-to-noise ratio of the clustering measurement, and the form adopted for the correlation function $\xi(r) \equiv (r/r_0)^{-\gamma}$ (such that amplitude and slope are not independent parameters), a strong degeneracy exists between r_0 and γ , such that neither is individually well determined.

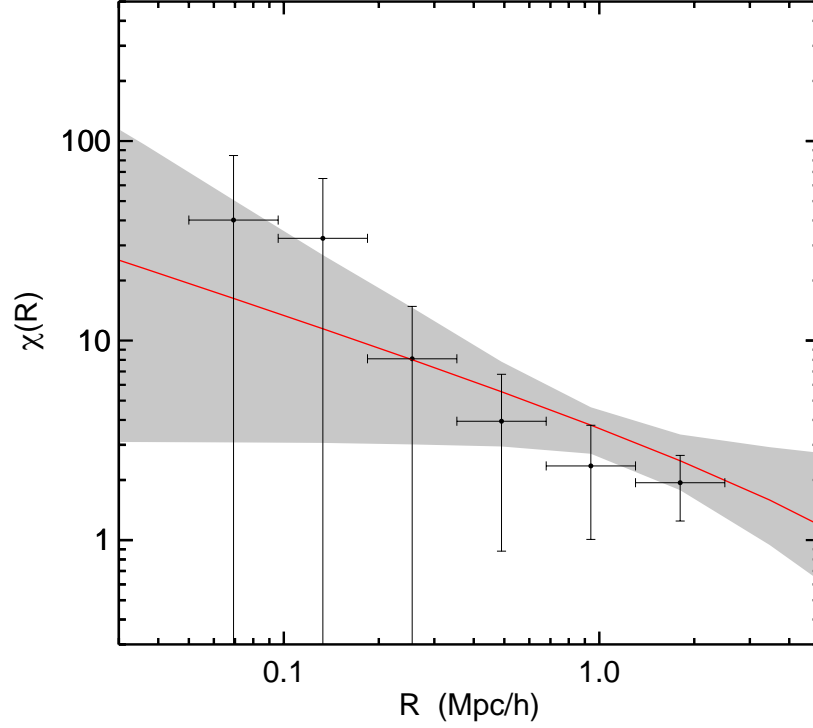


Fig. S5: Binned correlation function of LAEs around HzRGs and LABs. The dimensionless correlation function χ defined by eqn. (9) is indicated by the data points, with 1σ error bars, determined by taking the 16th and 84th percentiles of the distribution of χ resulting from our bootstrap procedure. The solid red line indicates the best-fit protocluster-LAE cross correlation function ($r_0 = 29.3 h^{-1} \text{ Mpc}$ and $\gamma = 1.5$) determined by our unbinned maximum likelihood procedure. The gray shaded region indicates the 1σ error on our cross-correlation function fit, implied by the errors on the parameters r_0 and γ . This region is determined by evaluating χ for each sample of the bootstrap error distributions of r_0 and γ , and taking the 16th to 84th percentile confidence region of χ . Our best fit correlation function (red line), and its quoted errors (gray shaded) clearly provides an acceptable representation of the binned data points and their respective errors.

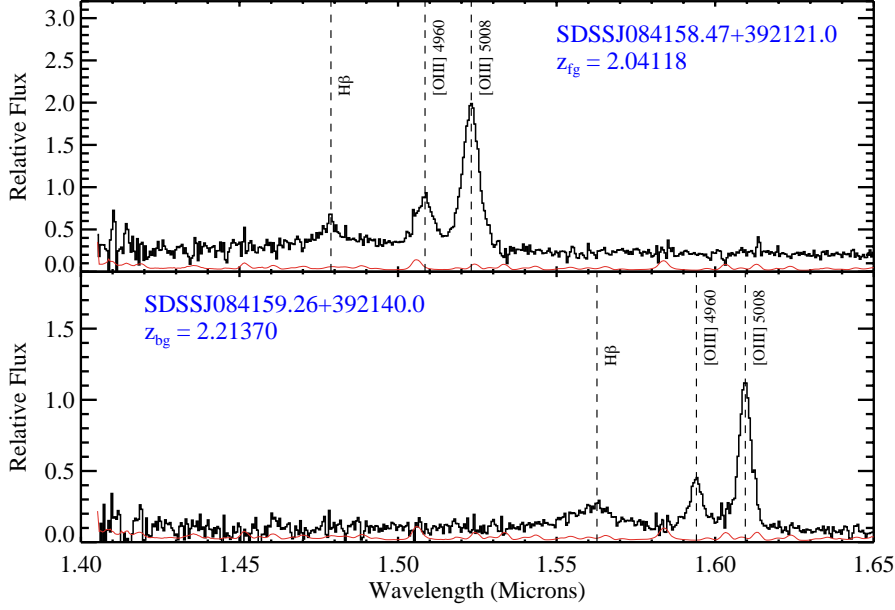


Fig. S6: Near-IR spectrum of the f/g quasar SDSSJ084158.47+392121.0 (top) and of the b/g quasar BOSSJ084159.26+392140.0 (bottom) obtained with the NIRI spectrometer on the Gemini-North telescope. Each quasar shows the detection of strong [O III] emission and modest $H\beta$ emission. The [O III] λ 5008Å doublet lines were centroided, giving observed wavelength centroids of $\lambda_{\text{obs}} = 1.5231 \pm 0.0001\mu\text{m}$ and $1.6095 \pm 0.00006\mu\text{m}$ for the f/g and b/g quasars respectively. This gives systemic redshifts $z_{\text{fg}} = 2.0418$ for the f/g quasar and 2.21370 for the b/g quasar. The estimated uncertainty on this redshift measurements is approximately 50 km s^{-1} , taking into account both the error in our wavelength calibration and the estimated uncertainty when one uses [O III] to assess the systemic redshift of a quasar. This uncertainty on the measurement of the redshift is far lower than the width of our custom narrow-band filter ($\sim 2600 \text{ km s}^{-1}$).

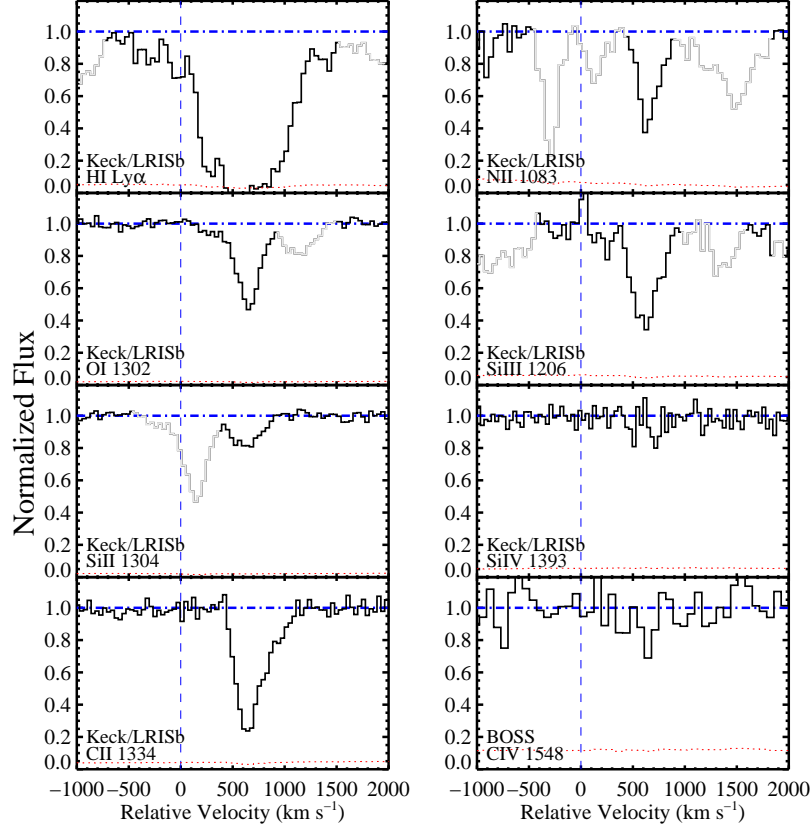


Fig. S7: One-dimensional spectra of the b/g quasar centered at the wavelengths of a series of commonly observed UV-line transitions in the rest frame of the f/g quasar. The gas exhibits especially strong low-ion absorption (O I λ 1302, Si II λ 1304, C II λ 1334) and moderately strong intermediate ion absorption (N II λ 1083, Si III λ 1206). The latter absorption occurs within the Ly α forest and could be partially blended with coincident IGM absorption, but such contamination should be modest given that the line-profiles track one another and also the low-ion transitions. In contrast, there is no statistically significant absorption corresponding to the Si IV λ 1393 and C IV λ 1548 transitions indicating the gas is not highly ionized. See Table S6 for a summary of the properties of these metal absorption lines.

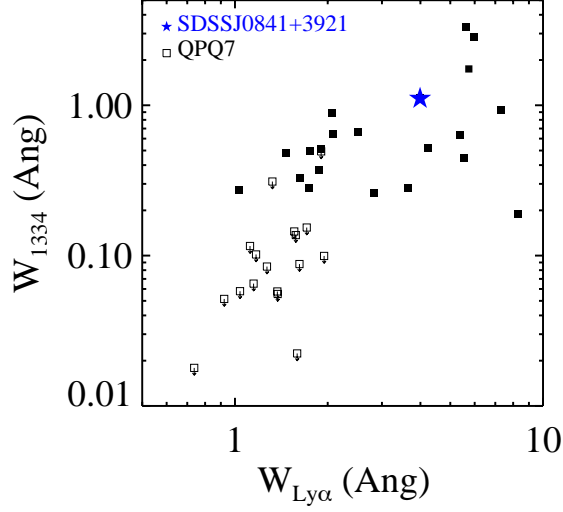


Fig. S8: Equivalent widths of cool gas absorption in the QPQ dataset. Measurements of the equivalent widths of the C II 1334 transition against the measurement for H I Ly α . The measurements are drawn from our QPQ survey (27, 28) and the pair that led to the serendipitous discovery of the quadruple AGN system is marked separately. The gas probed by the background quasar (at an impact parameter of 176 kpc) shows strong low-ion absorption characteristic of the full population. This indicates a highly enriched and optically thick gas.

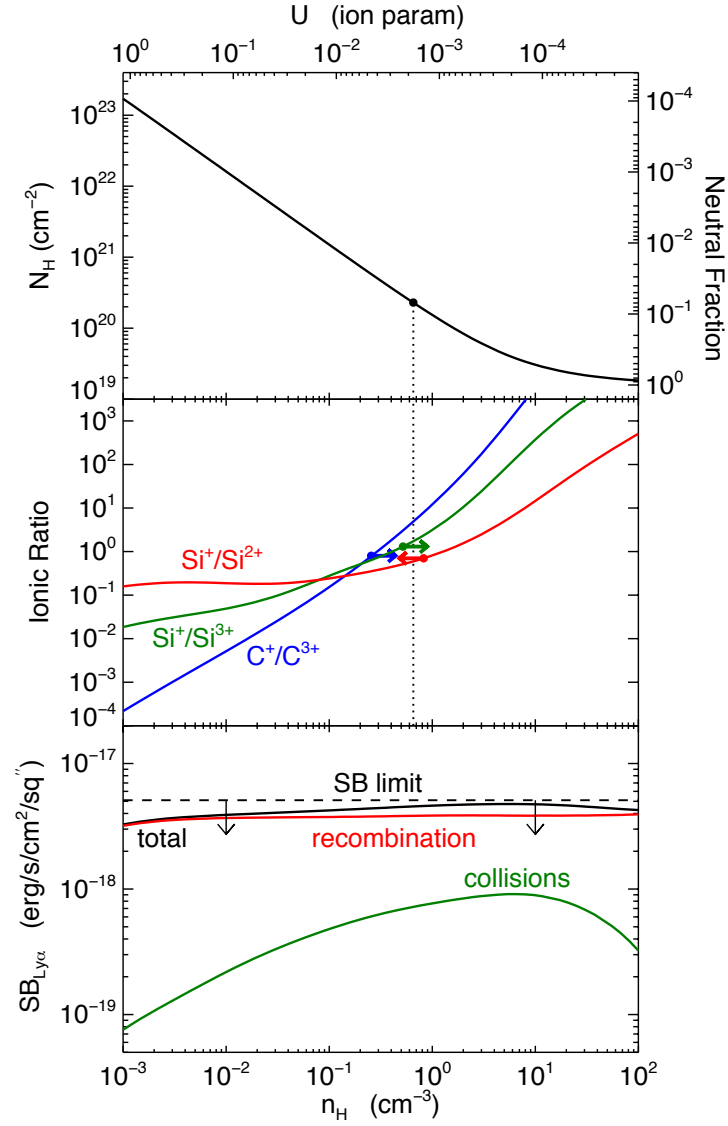


Fig. S9: Photoionization model of the optically thick absorber in b/g quasar spectrum. The gas is assumed to be at $r = 250$ kpc and exposed to the radiation field of the f/g quasar. The models are a one-dimensional sequence parameterized by the hydrogen volume density n_H on the x-axis, which given that the radiation field is fixed, is also a proxy for the ionization parameter U shown on the upper x-axis. Upper panel: Variation of the total hydrogen column N_H with n_H/U , given that we require the model to reproduce our measured neutral column density $N_{\text{HI}} = 10^{19.2}$. The y-axis on the right shows the corresponding neutral fraction. Our measured $\log_{10} U$ (middle panel) in turn implies $\log_{10} N_H = 20.4 \pm 0.4$, indicated by the vertical dotted line. Middle Panel: Variation of three different ionic ratios ($\text{Si}^+/\text{Si}^{2+}$ in red; $\text{Si}^+/\text{Si}^{3+}$ in green; C^+/C^{3+} in blue) with n_H/U . Our measured lower/upper limits on these ratios from Table S6 are illustrated by the colored arrows. We obtain a consistent photoionization solution implying $\log_{10} U = -2.7 \pm 0.3$, indicated by the vertical dotted line. Lower Panel: Predicted SB of extended Ly α emission from the absorbing gas as a function of n_H/U . The red and green curves show the respective contributions from recombinations and collisional excitation, and the black curve shows the total Ly α SB. The horizontal dashed line with arrows indicates our detection limit for an extended source near the b/g quasar sightline $\text{SB}_{\text{Ly}\alpha} < 5.1 \times 10^{-18} \text{ erg s}^{-1} \text{ cm}^{-2} \text{ arcsec}^{-2}$. If the absorbing gas is at $r = 250$ kpc as we have assumed, our models are marginally consistent with a non-detection of extended Ly α emission at that location. If the gas lies at larger distances $r > 250$ kpc, the predicted SB will decrease as r^{-2} .

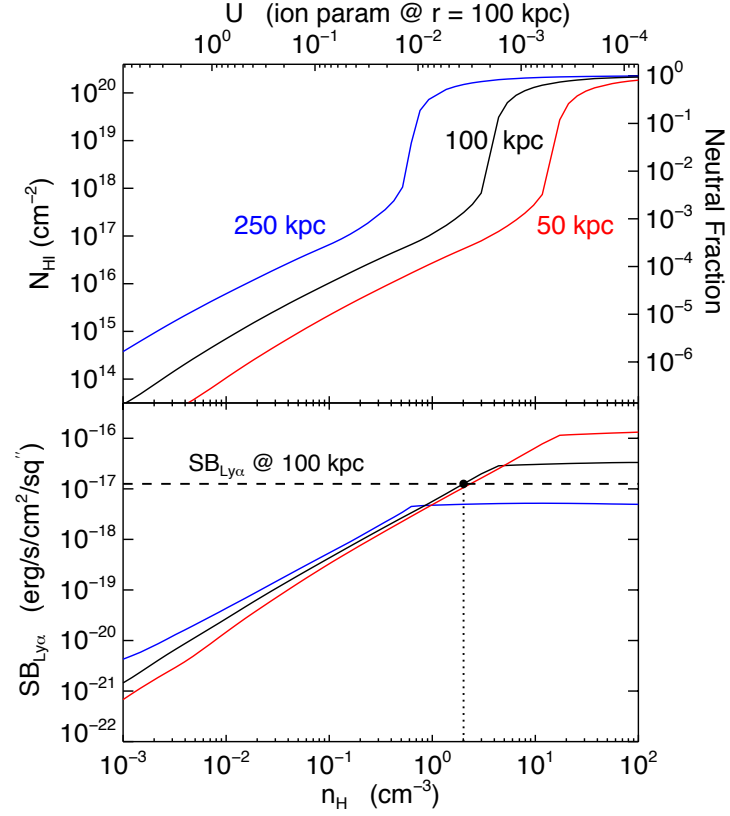


Fig. S10: Photoionization model of the Ly α emitting nebular gas. The models assume a total hydrogen column density $N_{\text{H}} = 10^{20.4} \text{ cm}^{-2}$, deduced from our photoionization modeling of the optically thick absorber in the b/g sightline (see Fig. S9 and § 10.3). The gas is assumed to be exposed to the radiation field of the f/g quasar at distances of $r = 50, 100$, and 250 kpc, indicated by the red, black, and blue curves, respectively. The models are parameterized by the hydrogen volume density n_{H} on the x-axis. The ionization parameter U corresponding to the gas at $r = 100$ kpc (black curves) is denoted on the upper x-axis. Upper panel: Variation of the neutral hydrogen column N_{HI} with n_{H} . The y-axis on the right shows the corresponding neutral fraction. Lower panel: Variation of the Ly α SB with n_{H} . For low n_{H} the gas remains optically thin $N_{\text{HI}} \lesssim 10^{17.5} \text{ cm}^{-2}$, and the SB $\text{SB}_{\text{Ly}\alpha}$ varies linearly with n_{H} and is nearly independent of the ionizing radiation intensity. At higher n_{H} the gas begins self-shielding $N_{\text{HI}} \gtrsim 10^{17.5} \text{ cm}^{-2}$, and the SB plateaus at a single value depending only on Φ and hence on distance r . The models indicate that a value of $n_{\text{H}} \simeq 2.0 \text{ cm}^{-3}$, indicated by the vertical dotted line, is required in order to reproduce the observed average emission level at 100 kpc of $\text{SB}_{\text{Ly}\alpha} = 1.3 \times 10^{-17} \text{ erg s}^{-1} \text{ cm}^{-2} \text{ arcsec}^{-2}$, indicated by the horizontal dashed line in Fig. S10. This conclusion is essentially independent of the radiation field and hence the assumed distance of the gas from the f/g quasar.

Name	RA	DEC	z	σ_z (km s ⁻¹)	θ ($''$)	R_\perp (kpc)
f/g QSO	08 41 58.47	+39 21 21.0	2.0412	50	—	—
AGN1	08 41 58.24	+39 21 29.1	2.055	400	8.6	71
AGN2	08 41 58.66	+39 21 14.7	2.058	700	6.6	55
AGN3	08 41 59.10	+39 21 04.6	2.050	700	18.0	150
b/g QSO	08 41 59.25	+39 21 40.0	2.2138	50	21.1	176

Table S1: AGN properties. The coordinates, redshift z , redshift error σ_z , angular θ and transverse separation R_\perp from the f/g quasar are listed for the four AGN in the protocluster, as well as the b/g quasar.

Name	$u \pm \sigma_u$	$g \pm \sigma_g$	$r \pm \sigma_r$	$i \pm \sigma_i$	$z \pm \sigma_z$	$W1 \pm \sigma_{W1}$	$W2 \pm \sigma_{W2}$	$W3 \pm \sigma_{W3}$	$W4 \pm \sigma_{W4}$	$F_{20\text{cm}}$	$V \pm \sigma_V$	$f_{\text{Ly}\alpha}$	$W_{\text{Ly}\alpha}$
f/g QSO	19.76 ± 0.02	19.75 ± 0.01	19.58 ± 0.01	19.27 ± 0.01	19.19 ± 0.03	15.85 ± 0.03	14.65 ± 0.04	10.79 ± 0.07	8.33 ± 0.36	< 1.02	19.76 ± 0.03	1709.0	72.6
AGN1	> 23.11	24.04 ± 0.31	> 23.74	> 23.24	> 21.86	16.89 ± 0.08	15.86 ± 0.11	> 12.58	> 8.36	< 1.02	23.95 ± 0.07	210.1	110.8
AGN2	> 23.11	> 24.34	> 23.40	> 22.93	> 21.86	18.19 ± 0.26	> 17.10	> 12.58	> 8.35	12.87	23.12 ± 0.06	41.1	37.0
AGN3	> 23.11	22.71 ± 0.09	22.73 ± 0.16	22.18 ± 0.15	> 21.86	> 18.52	> 17.12	> 12.58	> 8.36	< 1.02	23.09 ± 0.06	39.8	34.7
b/g QSO	20.00 ± 0.02	19.39 ± 0.00	19.71 ± 0.01	19.39 ± 0.01	19.39 ± 0.04	16.40 ± 0.05	15.76 ± 0.10	12.00 ± 0.21	> 8.36	< 1.02	19.96 ± 0.03	-7.0	-6.2

Table S2: AGN photometry. SDSS optical (*ugriz*) and WISE mid-IR (W1 – 4) magnitudes are determined from forced photometry of the corresponding images. SDSS and LRIS magnitudes are on the AB scale, whereas WISE magnitudes are in the Vega system. For measurements with $S/N < 3$ we quote lower limits on the magnitudes. Peak 20cm radio flux $F_{20\text{cm}}$ (mJy) are listed for objects with a match in the source catalog from the VLA/FIRST survey (Becker et al. 1995). For objects without FIRST matches we list the 5σ upper limit based on the sky-rms coverage maps. We also list Keck LRIS V band magnitudes, $\text{Ly}\alpha$ line fluxes $f_{\text{Ly}\alpha}$ ($10^{-17} \text{ erg s}^{-1} \text{ cm}^{-2}$), and rest-frame $\text{Ly}\alpha$ equivalent width (\AA).

Line	FWHM (km s ⁻¹)	Flux (10 ⁻¹⁷ erg s ⁻¹ cm ⁻²)	W_λ (Å)
Ly α	1575 \pm 36	76.5 \pm 1.5	> 118.2
NV.....	—	-0.4 \pm 1.4	—
CIV.....	—	1.3 \pm 0.8	—
HeII.....	1154 \pm 276	2.4 \pm 0.4	> 15.8
CIII].....	1434 \pm 171	2.6 \pm 0.3	22.6 \pm 2.2
CII].....	—	1.0 \pm 0.2	11.2 \pm 2.6

Table S3: Emission line measurements for the Type-2 quasar AGN1. Line fluxes were measured from the one-dimensional spectrum of the AGN, and errors determined from the 1σ noise vector. For lines detected at $S/N > 3$, rest-frame equivalent widths W_λ are computed. If the continuum lies above the 1σ noise vector these are listed as values, otherwise we quote lower limits. The FWHM for emission lines for which our discovery spectra had sufficient S/N for a measurement (Ly α , He II, and C III]) are also listed.

Tag	RA	DEC	$f_{\text{Ly}\alpha}$ (10^{-17} ergs $^{-1}$ cm $^{-2}$)	f_{λ} (10^{-19} ergs $^{-1}$ cm $^{-2}$ Å $^{-1}$)	$W_{\text{Ly}\alpha}$ (Å)	R_{\perp} (kpc)
f/g QSO	08:41:58.470	+39:21:20.97	1708.76	774.23	72.61	0
AGN2*	08:41:58.685	+39:21:15.00	41.13	36.57	36.98	50
*	08:41:57.982	+39:21:25.88	12.07	2.04	195.0	58
	08:41:58.872	+39:21:14.45	4.14	3.38	40.28	62
AGN1*	08:41:58.238	+39:21:28.87	210.08	62.35	110.80	65
	08:41:57.535	+39:21:17.72	1.33	0.41	106.14	88
*	08:41:58.543	+39:21:34.03	21.45	14.42	48.91	102
*	08:41:58.262	+39:21:37.57	14.07	3.97	116.50	130
AGN3*	08:41:59.107	+39:21:04.67	39.81	37.76	34.67	139
*	08:41:58.286	+39:21:39.20	4.33	0.95	148.98	143
	08:41:58.238	+39:20:57.05	3.42	5.10	22.06	187
	08:41:59.035	+39:21:46.27	1.72	1.09	52.02	203
	08:41:57.019	+39:21:48.45	1.13	0.46	80.45	251
Target1*	08:41:58.824	+39:21:57.42	17.22	5.86	96.66	285
	08:41:59.762	+39:21:55.52	0.69	0.14	157.38	293
	08:41:55.754	+39:21:46.27	0.86	0.99	28.70	314
	08:41:54.958	+39:21:14.99	1.30	0.49	87.57	321
	08:41:56.198	+39:21:55.51	0.78	0.82	31.32	338
	08:41:53.926	+39:21:33.75	0.72	0.52	45.52	422
	08:41:54.982	+39:20:41.54	0.85	0.65	43.33	440
	08:41:59.038	+39:20:20.88	1.63	2.77	19.42	470
	08:41:59.225	+39:20:21.16	0.85	1.10	25.30	470
	08:41:56.762	+39:20:19.79	0.54	0.89	20.02	500
	08:42:02.412	+39:20:30.94	0.93	1.49	20.44	527
	08:41:57.794	+39:20:11.63	1.12	1.56	23.56	543
*	08:41:52.003	+39:21:14.16	5.31	3.44	50.73	586
	08:41:52.142	+39:21:48.16	1.21	0.82	48.76	609
	08:41:55.778	+39:20:03.75	0.63	0.63	33.07	648
	08:42:02.225	+39:20:09.46	0.96	0.30	105.43	651
	08:42:02.412	+39:20:06.74	0.99	0.98	32.99	678
*	08:41:52.802	+39:20:21.41	7.38	3.22	75.25	690
	08:42:05.930	+39:22:09.65	0.82	1.34	20.01	772
	08:41:58.027	+39:23:01.05	0.66	0.80	27.08	779
	08:41:52.099	+39:20:11.62	1.86	1.28	47.73	788
	08:41:51.722	+39:20:16.51	0.74	0.19	126.03	789
	08:42:07.313	+39:21:23.42	0.56	0.91	20.07	798
	08:41:49.610	+39:21:22.58	0.55	0.85	21.21	800
	08:42:05.486	+39:22:24.88	0.59	0.65	29.80	805
	08:41:51.209	+39:20:17.33	0.68	0.30	75.60	821
	08:41:51.701	+39:20:08.90	0.62	0.68	30.16	829
	08:41:59.340	+39:23:07.04	0.61	0.80	25.07	829
	08:42:07.829	+39:21:32.66	0.92	1.10	27.59	849
	08:41:51.701	+39:20:01.01	0.92	1.33	22.82	872
	08:41:50.482	+39:20:10.25	0.67	0.66	33.42	907
	08:41:51.067	+39:20:02.09	0.96	0.11	282.90	907
	08:41:54.461	+39:23:11.92	0.91	0.97	30.68	936
	08:41:49.982	+39:22:30.30	0.66	0.85	25.42	937
	08:42:08.441	+39:22:05.84	1.71	1.33	42.09	964
	08:42:07.826	+39:20:09.72	0.73	0.69	34.54	1010
	08:42:10.267	+39:21:13.89	0.70	0.60	38.54	1065
	08:41:51.482	+39:23:15.72	0.62	0.92	22.36	1093
	08:42:10.759	+39:21:24.49	0.66	0.25	87.20	1109
	08:42:10.010	+39:22:10.45	2.21	0.27	268.26	1110
	08:42:12.590	+39:21:39.16	2.09	1.83	37.44	1281
	08:42:13.382	+39:20:05.34	11.69	4.20	91.60	1468
	08:42:11.702	+39:23:13.80	1.11	0.73	49.85	1481
	08:42:12.840	+39:19:12.32	0.82	0.62	43.35	1638
	08:42:03.629	+39:17:19.50	2.27	1.16	64.47	1935
	08:41:52.363	+39:17:15.40	1.35	1.44	30.75	1988
	08:42:03.677	+39:17:02.64	1.22	0.65	61.92	2064
	08:42:12.223	+39:16:41.66	2.61	2.83	30.30	2502

Table S4: Properties of the candidate LAEs around the f/g quasar. Here $f_{\text{Ly}\alpha}$ is the Ly α line flux in 10^{-17} erg s $^{-1}$ cm $^{-2}$, f_{λ} is the flux density in the continuum in units of 10^{-19} erg s $^{-1}$ cm $^{-2}$ Å $^{-1}$ estimated from the V-band, $W_{\text{Ly}\alpha}$ is the rest-frame Ly α equivalent width, and R_{\perp} the proper projected distance from the f/g quasar in kpc. LAEs are selected using the procedure described in § 4.1, namely they are required to have $W_{\text{Ly}\alpha} > 20\text{\AA}$ and $f_{\text{Ly}\alpha} > 5.4 \times 10^{-18}$ erg s $^{-1}$. Objects which were used to measure the overdensity profile around the f/g quasar in Fig. 2 are denoted by a * in the column Tag, where the name of the source is also indicated. These sources had to satisfy a brighter flux limit, namely $f_{\text{Ly}\alpha} > 4.0 \times 10^{-17}$ erg s $^{-1}$ cm $^{-2}$, and lie within 2.08' of the f/g quasar.

Name	Type	RA	DEC	z	Filter FWHM (\AA)	EW_{limit} (\AA)	Reference
MRC 2048–272	HzRG	20 51 03.5	–27 03 04.1	2.06	73	20	1
MRC 1138–262	HzRG	11 40 48.2	–26 29 09.5	2.16	65	20	1
LABd05	LAB	14 34 11.0	+33 17 32.6	2.66	201	40	2
MRC 0052241	HzRG	00 54 29.8	–23 51 31.1	2.86	66	20	1
MRC 0943–242	HzRG	09 45 32.7	–24 28 49.7	2.92	68	20	1
LAB1	LAB	22 17 26.0	+00 12 37.7	3.10	80	20	3
MRC 0316–257	HzRG	03 18 12.0	–25 35 10.8	3.13	59	20	1
TN J2009–3040	HzRG	20 09 48.1	–30 40 07.4	3.16	59	20	1

Table S5: Properties of objects analyzed in our protocluster-LAE correlation analysis. The nature of the source (HzRG or LAB), coordinates, redshift z , the FWHM of the NB filter used (\AA), the limiting EW of the LAE search (W_{limit}), and the reference for the observations are indicated. References used are: (1) Venemans et al. 2007 (*13*); (2) Prescott et al. 2008 (*19*); (3) Nestor et al. 2011 (*106*).

Ion	λ (Å)	$\log f$	v_{int} (km s ⁻¹)	W_λ (mÅ)	$\log N$	[X/H]
H 1	1215.6701	-0.3805	[-225, 1449]	3750.0 ± 50.0	19.2 ± 0.3	
C 2	1334.5323	-0.8935	[355, 1315]	1110.5 ± 34.7	> 14.7	> -1.19
C 4	1548.1949	-0.7194	[355, 1315]	< 331.5	< 13.9	< 0.72
	1550.7700	-1.0213	[355, 1315]	< 340.4	< 14.2	< 1.03
N 2	1083.9900	-0.9867	[480, 850]	216.3 ± 31.8	> 14.3	> -1.00
O 1	1302.1685	-1.3110	[355, 985]	672.9 ± 14.0	> 15.0	> -0.95
Al 2	1670.7874	0.2742	[355, 1315]	335.0 ± 110.0	> 12.9	> -0.97
Si 2	1304.3702	-1.0269	[431, 1315]	259.3 ± 17.5	> 14.3	> -0.81
Si 3	1206.5000	0.2201	[355, 1315]	951.0 ± 43.6	> 13.6	> -0.80
Si 4	1393.7550	-0.2774	[355, 1315]	< 96.2	< 13.0	< -0.27
	1402.7700	-0.5817	[355, 1315]	< 93.7	< 13.3	< 0.02

Table S6: Absorption line measurements. The columns indicate the Ion, rest wavelength λ , oscillator strength $\log f$, velocity interval v_{int} used for the calculation of the rest equivalent widths, rest-equivalent width W_λ , ionic column density N , and elemental abundances [X/H] implied by each metal absorption line measurement. The column densities N reported assume the linear curve-of-growth approximation. The metal abundances [X/H] are computed using ionization corrections from our favored Cloudy model presented in Section S10, and are reported according to the standard convention of logarithmic relative to Solar (i.e. 0 = solar abundance).

References and Notes

1. J. Magorrian, *et al.*, *AJ* **115**, 2285 (1998).
2. L. Ferrarese, *ApJ* **578**, 90 (2002).
3. J. N. Bahcall, S. Kirhakos, D. H. Saxe, D. P. Schneider, *ApJ* **479**, 642 (1997).
4. M. G. Haehnelt, M. J. Rees, *MNRAS* **263**, 168 (1993).
5. S. Djorgovski, *The Space Distribution of Quasars*, D. Crampton, ed. (1991), vol. 21 of *Astronomical Society of the Pacific Conference Series*, pp. 349–353.
6. J. F. Hennawi, *et al.*, *AJ* **131**, 1 (2006).
7. S. G. Djorgovski, *et al.*, *ApJL* **662**, L1 (2007).
8. E. P. Farina, C. Montuori, R. Decarli, M. Fumagalli, *MNRAS* **431**, 1019 (2013).
9. C. Lacey, S. Cole, *MNRAS* **262**, 627 (1993).
10. R. F. Trainor, C. C. Steidel, *ApJ* **752**, 39 (2012).
11. M. White, *et al.*, *MNRAS* **424**, 933 (2012).
12. N. Fanidakis, A. V. Macciò, C. M. Baugh, C. G. Lacey, C. S. Frenk, *MNRAS* **436**, 315 (2013).
13. B. P. Venemans, *et al.*, *A & A* **461**, 823 (2007).
14. P. J. Francis, *et al.*, *ApJ* **457**, 490 (1996).
15. C. C. Steidel, *et al.*, *ApJ* **532**, 170 (2000).
16. A. Dey, *et al.*, *ApJ* **629**, 654 (2005).
17. R. A. Overzier, *et al.*, *ApJ* **771**, 89 (2013).
18. M. K. M. Prescott, I. Momcheva, G. B. Brammer, J. P. U. Fynbo, P. Møller, *ArXiv e-prints* (2015).
19. M. K. M. Prescott, N. Kashikawa, A. Dey, Y. Matsuda, *ApJL* **678**, L77 (2008).
20. Y. Yang, A. Zabludoff, C. Tremonti, D. Eisenstein, R. Davé, *ApJ* **693**, 1579 (2009).
21. Y.-K. Chiang, R. Overzier, K. Gebhardt, *ApJ* **779**, 127 (2013).
22. J. F. Hennawi, J. X. Prochaska, *ApJ* **766**, 58 (2013).
23. J. F. Hennawi, *et al.*, *ApJ* **651**, 61 (2006).
24. J. F. Hennawi, J. X. Prochaska, *ApJ* **655**, 735 (2007).
25. J. X. Prochaska, J. F. Hennawi, *ApJ* **690**, 1558 (2009).
26. J. X. Prochaska, J. F. Hennawi, R. A. Simcoe, *ApJL* **762**, L19 (2013).
27. J. X. Prochaska, *et al.*, *ApJ* **776**, 136 (2013).
28. J. X. Prochaska, M. W. Lau, J. F. Hennawi, *ApJ* **796**, 140 (2014).
29. See further information in supplementary online material § S2 on *Science Online*.
30. I. Kayo, M. Oguri, *MNRAS* **424**, 1363 (2012).
31. See further information in supplementary online material § S3 on *Science Online*.
32. R. Ciardullo, *et al.*, *ApJ* **744**, 110 (2012).

33. See further information in supplementary online material § S4 on *Science Online*.
34. See further information in supplementary online material § S6 on *Science Online*.
35. See further information in supplementary online material § S5 on *Science Online*.
36. B. D. Lehmer, *et al.*, *ApJ* **691**, 687 (2009).
37. See further information in supplementary online material § S7 on *Science Online*.
38. R. E. Mostardi, *et al.*, *ApJ* **779**, 65 (2013).
39. D. C. Martin, *et al.*, *ApJ* **786**, 106 (2014).
40. See further information in supplementary online material § S8 on *Science Online*.
41. S. Cantalupo, F. Arrigoni-Battaia, J. X. Prochaska, J. F. Hennawi, P. Madau, *Nature* **506**, 63 (2014).
42. M. Fumagalli, *et al.*, *ApJ* **780**, 74 (2014).
43. C.-A. Faucher-Giguere, *et al.*, *ArXiv e-prints* (2014).
44. S. Lopez, *et al.*, *ApJ* **679**, 1144 (2008).
45. See further information in supplementary online material § S9 on *Science Online*.
46. See further information in supplementary online material § S10 on *Science Online*.
47. N. H. M. Crighton, *et al.*, *ArXiv e-prints* (2014).
48. A. H. Maller, J. S. Bullock, *MNRAS* **355**, 694 (2004).
49. H. J. Mo, J. Miralda-Escude, *ApJ* **469**, 589 (1996).
50. T. M. Heckman, S. A. Baum, W. J. M. van Breugel, P. McCarthy, *ApJ* **338**, 48 (1989).
51. M. McDonald, S. Veilleux, D. S. N. Rupke, R. Mushotzky, *ApJ* **721**, 1262 (2010).
52. K. N. Abazajian, *et al.*, *ApJS* **182**, 543 (2009).
53. J. F. Hennawi, *et al.*, *ApJ* **719**, 1672 (2010).
54. C. P. Ahn, *et al.*, *ApJS* **203**, 21 (2012).
55. J. B. Oke, *et al.*, *PASP* **107**, 375 (1995).
56. E. Bertin, S. Arnouts, *A&AS* **117**, 393 (1996).
57. E. Bertin, *Astronomical Data Analysis Software and Systems XV*, C. Gabriel, C. Arviset, D. Ponz, S. Enrique, eds. (2006), vol. 351 of *Astronomical Society of the Pacific Conference Series*, p. 112.
58. E. Bertin, *et al.*, *Astronomical Data Analysis Software and Systems XI*, D. A. Bohlender, D. Durand, T. H. Handley, eds. (2002), vol. 281 of *Astronomical Society of the Pacific Conference Series*, p. 228.
59. J. B. Oke, *AJ* **99**, 1621 (1990).
60. A. U. Landolt, *AJ* **104**, 372 (1992).
61. S. Cantalupo, S. J. Lilly, M. G. Haehnelt, *MNRAS* **425**, 1992 (2012).
62. S. M. Faber, *et al.*, *Instrument Design and Performance for Optical/Infrared Ground-based Telescopes*, M. Iye, A. F. M. Moorwood, eds. (2003), vol. 4841 of *Society of Photo-Optical Instrumentation Engineers (SPIE) Conference Series*, pp. 1657–1669.
63. J. A. Newman, *et al.*, *ApJS* **208**, 5 (2013).

64. M. C. Cooper, J. A. Newman, M. Davis, D. P. Finkbeiner, B. F. Gerke, spec2d: DEEP2 DEIMOS Spectral Pipeline, Astrophysics Source Code Library (2012).
65. D. Lang, D. W. Hogg, D. J. Schlegel, *ArXiv e-prints* (2014).
66. A. E. Shapley, C. C. Steidel, M. Pettini, K. L. Adelberger, *ApJ* **588**, 65 (2003).
67. R. Antonucci, *ARAA* **31**, 473 (1993).
68. C. M. Urry, P. Padovani, *PASP* **107**, 803 (1995).
69. D. B. Sanders, *et al.*, *ApJ* **325**, 74 (1988).
70. P. J. McCarthy, *ARAA* **31**, 639 (1993).
71. M. Lacy, *et al.*, *ApJS* **154**, 166 (2004).
72. D. Stern, *et al.*, *ApJ* **631**, 163 (2005).
73. W. N. Brandt, G. Hasinger, *ARAA* **43**, 827 (2005).
74. N. L. Zakamska, *et al.*, *AJ* **126**, 2125 (2003).
75. M. Brusa, *et al.*, *ApJ* **716**, 348 (2010).
76. L. Hao, *et al.*, *AJ* **129**, 1783 (2005).
77. M. Kim, *et al.*, *ApJL* **768**, L9 (2013).
78. D. Stern, *et al.*, *ApJ* **568**, 71 (2002).
79. B. A. Groves, M. A. Dopita, R. S. Sutherland, *ApJS* **153**, 75 (2004).
80. C. De Breuck, H. Röttgering, G. Miley, W. van Breugel, P. Best, *A & A* **362**, 519 (2000).
81. T. Nagao, R. Maiolino, A. Marconi, *A & A* **447**, 863 (2006).
82. K. N. Hainline, A. E. Shapley, J. E. Greene, C. C. Steidel, *ApJ* **733**, 31 (2011).
83. M. Lacy, *et al.*, *ApJS* **208**, 24 (2013).
84. D. E. Vanden Berk, *et al.*, *AJ* **122**, 549 (2001).
85. T. Nagao, A. Marconi, R. Maiolino, *A & A* **447**, 157 (2006).
86. W. Zheng, G. A. Kriss, R. C. Telfer, J. P. Grimes, A. F. Davidsen, *ApJ* **475**, 469 (1997).
87. D. Stern, *et al.*, *ApJ* **753**, 30 (2012).
88. R. J. Assef, *et al.*, *ApJ* **772**, 26 (2013).
89. L. Yan, *et al.*, *AJ* **145**, 55 (2013).
90. M. Polletta, *et al.*, *ApJ* **663**, 81 (2007).
91. R. J. Assef, *et al.*, *ApJ* **713**, 970 (2010).
92. R. C. Hickox, *et al.*, *ApJ* **671**, 1365 (2007).
93. R. C. Hickox, *et al.*, *ApJ* **731**, 117 (2011).
94. Y. Shen, *et al.*, *AJ* **133**, 2222 (2007).
95. R. H. Becker, R. L. White, D. J. Helfand, *ApJ* **450**, 559 (1995).
96. F. M. Montenegro-Montes, *et al.*, *MNRAS* **388**, 1853 (2008).

97. M. A. DiPompeo, M. S. Brotherton, C. De Breuck, S. Laurent-Muehleisen, *ApJ* **743**, 71 (2011).
98. S. Fine, M. J. Jarvis, T. Mauch, *MNRAS* **412**, 213 (2011).
99. P. J. E. Peebles, *The large-scale structure of the universe* (Princeton University Press, 1980).
100. J. N. Fry, *ApJ* **279**, 499 (1984).
101. A. Cooray, R. Sheth, *Physics Reports* **372**, 1 (2002).
102. P. F. Hopkins, G. T. Richards, L. Hernquist, *ApJ* **654**, 731 (2007).
103. R. Reyes, *et al.*, *AJ* **136**, 2373 (2008).
104. E. Lusso, *et al.*, *ApJ* **777**, 86 (2013).
105. E. Bertin, S. Arnouts, *Astronomy and Astrophysics Supplement* **117**, 393 (1996).
106. D. B. Nestor, A. E. Shapley, C. C. Steidel, B. Siana, *ApJ* **736**, 18 (2011).
107. R. A. C. Croft, G. B. Dalton, G. Efstathiou, W. J. Sutherland, S. J. Maddox, *MNRAS* **291**, 305 (1997).
108. Y. Shen, *et al.*, *ApJ* **719**, 1693 (2010).
109. L. Guaita, *et al.*, *ApJ* **733**, 114 (2011).
110. K. L. Adelberger, C. C. Steidel, *ApJL* **627**, L1 (2005).
111. G. T. Richards, *et al.*, *AJ* **124**, 1 (2002).
112. R. van Ojik, *et al.*, *A & A* **313**, 25 (1996).
113. M. Villar-Martín, *et al.*, *MNRAS* **346**, 273 (2003).
114. M. Villar-Martín, *New A Rev.* **51**, 194 (2007).
115. A. Humphrey, *et al.*, *MNRAS* **375**, 705 (2007).
116. M. K. M. Prescott, C. L. Martin, A. Dey, *ApJ* **799**, 62 (2015).
117. T. M. Heckman, G. K. Miley, M. D. Lehnert, W. van Breugel, *ApJ* **370**, 78 (1991).
118. R. Trainor, C. C. Steidel, *ApJL* **775**, L3 (2013).
119. G. Miley, C. De Breuck, *A&A Rev.* **15**, 67 (2008).
120. K. K. Nilsson, J. P. U. Fynbo, P. Møller, J. Sommer-Larsen, C. Ledoux, *A & A* **452**, L23 (2006).
121. D. J. B. Smith, M. J. Jarvis, *MNRAS* **378**, L49 (2007).
122. T. M. A. Webb, *et al.*, *ApJ* **692**, 1561 (2009).
123. J. W. Colbert, *et al.*, *ApJ* **728**, 59 (2011).
124. J. X. Prochaska, H.-W. Chen, A. M. Wolfe, M. Dessauges-Zavadsky, J. S. Bloom, *ApJ* **672**, 59 (2008).
125. G. E. Prochter, J. X. Prochaska, J. M. O'Meara, S. Burles, R. A. Bernstein, *ApJ* **708**, 1221 (2010).
126. G. J. Ferland, *et al.*, *PASP* **110**, 761 (1998).
127. A. Gould, D. H. Weinberg, *ApJ* **468**, 462 (1996).
128. E. Lusso, *et al.*, *ArXiv e-prints* (2015).
129. F. Arrigoni Battaia, *et al.*, *ArXiv e-prints* (2014).
130. I. V. Strateva, W. N. Brandt, D. P. Schneider, D. G. Vanden Berk, C. Vignali, *AJ* **130**, 387 (2005).
131. G. T. Richards, *et al.*, *ApJS* **166**, 470 (2006).
132. A. Baskin, A. Laor, J. Stern, *MNRAS* **438**, 604 (2014).
133. F. Haardt, P. Madau, *ApJ* **746**, 125 (2012).